JOURNAL OF GEOPHYSICAL RESEARCH, VOL. 114, B07405, doi:10.1029/2008JB005748, 2009

Postseismic deformation due to the M_w 6.0 2004 Parkfield earthquake: Stress-driven creep on a fault with spatially variable rate-and-state friction parameters

Sylvain Barbot,[1] Yuri Fialko,[1] and Yehuda Bock[1]

Received 15 April 2008; revised 6 March 2009; accepted 27 April 2009; published 18 July 2009.

[1] We investigate the coseismic and postseismic deformation due to the M_w 6.0 2004 Parkfield, California, earthquake. We produce coseismic and postseismic slip models by inverting data from an array of 14 continuous GPS stations from the SCIGN network. Kinematic inversions of postseismic GPS data over a time period of 3 years show that afterslip occurred in areas of low seismicity and low coseismic slip, predominantly at a depth of ~5 km. Inversions suggest that coseismic stress increases were relaxed by predominantly aseismic afterslip on a fault plane. The kinetics of afterslip is consistent with a velocity-strengthening friction generalized to include the case of infinitesimal velocities. We performed simulations of stress-driven creep using a numerical model that evaluates the time-dependent deformation due to coseismic stress changes in a viscoelastoplastic half-space. Starting with a coseismic slip distribution, we compute the time-dependent evolution of afterslip on a fault plane and the associated displacements at the GPS stations. Data are best explained by a rate-strengthening model with frictional parameter $(a - b) = 7 \times 10^{-3}$, at a high end of values observed in laboratory experiments. We also find that the geodetic moment due to creep is a factor of 100 greater than the cumulative seismic moment of aftershocks. The rate of aftershocks in the top 10 km of the seismogenic zone mirrors the kinetics of afterslip, suggesting that postearthquake seismicity is governed by loading from the nearby aseismic creep. The San Andreas fault around Parkfield is deduced to have large along-strike variations in rate-and-state frictional properties. Velocity strengthening areas may be responsible for the separation of the coseismic slip in two distinct asperities and for the ongoing aseismic creep occurring between the velocity-weakening patches after the 2004 rupture.

Citation: Barbot, S., Y. Fialko, and Y. Bock (2009), Postseismic deformation due to the M_w 6.0 2004 Parkfield earthquake: Stress-driven creep on a fault with spatially variable rate-and-state friction parameters, *J. Geophys. Res.*, *114*, B07405, doi:10.1029/2008JB005748.

1. Introduction

[2] The San Andreas fault around Parkfield, California, exhibits a transition from a creeping segment to the northwest to a locked segment to the southeast. The creeping section experiences a quasi-steady sliding at a rate of 33 mm/a [*Murray et al.*, 2001], close to the estimated 35 mm/a long-term rate of the San Andreas fault at that latitude [*Lisowski et al.*, 1991]. Moderate magnitude 6 earthquakes repeatedly occur in this transition zone. The 2004 M_w 6.0 Parkfield earthquake is the most recent in a series of events including a least five historical earthquakes in 1881, 1901, 1922, 1934, and 1966 rupturing approximately the same area on the fault [*Bakun and McEvilly*, 1984; *Bakun et al.*, 2005]. The Earthquake Prediction Experiment [*Bakun and Lindh*, 1985], motivated by the small recurrence time of the Parkfield sequence, sought to monitor the anticipated earthquake and reveal the earthquake process in unprecedented detail. The event of 28 September 2004 was the subject of numerous studies that exploited a large variety of available geophysical data [e.g., *Harris and Arrowsmith*, 2006].

[3] The coseismic rupture was imaged using various geodetic [e.g., *Johanson et al.*, 2006; *Johnson et al.*, 2006; *Langbein et al.*, 2006] and seismic [e.g., *Liu et al.*, 2006; *Allmann and Shearer*, 2007] observations. A common feature of these studies is the partition of the earthquake slip distribution in two distinct areas of high slip: a first patch located close to the epicenter, and a second, larger amplitude patch, farther to the northwest. Previous studies showed that the postseismic transient is likely dominated by afterslip [e.g., *Johanson et al.*, 2006; *Johnson et al.*,

[1]Institute of Geophysics and Planetary Physics, Scripps Institution of Oceanography, University of California, San Diego, La Jolla, California, USA.

0148-0227/09/2008JB005748$09.00

2006; *Freed*, 2007]. *Johanson et al.* [2006] inferred the details of the early afterslip distribution from GPS and interferometric synthetic aperture radar (InSAR) measurements. Somewhat surprisingly, more fault-averaged slip was found to have occurred during the postseismic period than during the coseismic rupture. The inferred geodetic moment due to afterslip was equivalent to a magnitude M_w 6.1 earthquake over four months following the rupture [*Johanson et al.*, 2006], and M_w 6.3 2 years after the event [*Freed*, 2007] (i.e., about 3 times the coseismic moment release). The moment release during coseismic and postseismic slip differs from that observed in other instrumented areas and might be peculiar because of the transition between the creeping and locked segments of the San Andreas fault.

[4] In this study, we take advantage of the continuous GPS array of the SCIGN network [*Langbein and Bock*, 2004], which covers the Parkfield segment during the interseismic, coseismic, and postseismic intervals, to constrain the dominant mechanisms driving the postseismic deformation over 3 years following the 2004 earthquake. In section 2, we begin by deriving a coseismic slip model and estimating the resolving power of the GPS array. In section 3, we perform a series of kinematic inversions to track the evolution of slip on the fault plane over 3 years following the earthquake. In section 4, we describe stress-driven creep models incorporating power law and velocity-strengthening friction laws. We perform a principal component analysis of the GPS time series. We fit the dominant mode to analytic solutions for the postseismic relaxation of a simple creeping patch. In section 5, we use stress-driven creep models to constrain constitutive properties of the fault interface [*Stuart and Tullis*, 1995; *Johnson et al.*, 2006; *Perfettini and Avouac*, 2004, 2007]. We explore predictions of the rate- and state-dependent friction [*Dieterich*, 1992, 1994] using a new semianalytic model of nonlinear fault creep. Using our kinematically inferred coseismic slip distribution as an initial condition, we compute forward models of fault brittle creep and discuss implications for in situ constitutive frictional properties of rocks in the San Andreas fault zone. In Appendix A, we derive the analytic impulse response of a power law shear zone and of a rate-strengthening (RS) crack due to coseismic stress change. In Appendix B we describe our mathematical approach to model three-dimensional deformation due to nonlinear creep and present our numerical implementation. The rate of creep of the RS crack in the interseismic period is discussed in Appendix C.

2. Coseismic Slip Model

[5] We use the 28 September 2004, 1 day static offsets in the SCIGN continuous GPS time series computed at the Scripps Orbit and Permanent Array Center (http://sopac.ucsd.edu/) to invert for a coseismic slip distribution. We approximate the fault zone with a single fault segment and allow for right-lateral strike slip only. We discretize a 40 km long, 15 km deep plane with 2×1 km patches in the strike and dip directions, respectively. As inversions of surface displacements are intrinsically nonunique [e.g., *Parker*, 1994; *Mavko*, 1981; *Savage*, 1990], we impose slip nonnegativity, a smoothness constraint and zero slip at the bottom of the fault to regularize the problem (see *Fialko* [2004a] for details). In particular, we use the homogeneous elastic Green function [*Okada*, 1992] for a Poisson solid and the finite difference approximation of the gradient operator to smooth the slip model.

[6] We determine our preferred source geometry by performing a grid search for the strike, dip and position of the fault that best fit the GPS offsets. Figure 1 shows our best model, corresponding to a vertical fault striking N136°. Effects of the smoothness factor (SF) on the inferred geometry are illustrated in Figure 2. For high values of SF, the inferred slip distribution on the fault is smooth (see slip model in Figure 2a, top left). At intermediate values of SF, the slip distribution becomes bimodal, with two distinct slip patches appearing along strike. For smaller values of SF, the two slip patches persist and become more localized with a smaller slip area and a higher slip amplitude. We choose our smoothing factor $SF = 10^{-4}$ to be at the position where misfit is weakly dependent upon the degree of smoothing, as illustrated by the smoothness/misfit curve of Figure 2b. Using a uniform shear modulus of $G = 30$ GPa, our best fitting coseismic model has a geodetic moment of $m = 1.98 \times 10^{18}$ N equivalent to moment magnitude M_w 6.16, somewhat higher than the seismic moment of M_w 6.0. Inversions using a high-rate GPS data and a smaller coseismic interval gave rise to a geodetic moment of M_w 6.0, in a better agreement with estimates from seismic data [*Murray and Langbein*, 2006]. Our use of daily GPS solutions may include some early afterslip in the coseismic model. Figure 1b shows the modeled surface displacements at the 14 GPS stations, along with the GPS measurements and their two-sigma uncertainty. Most of the GPS displacements can be explained by right-lateral strike slip on the fault plane.

[7] The station distribution in the GPS array and the geometry of the fault limit our ability to infer slip equally well everywhere on the fault plane. Following the approach of *Backus* [1970] and *Tarantola* [2004], the resolution kernel of the underdetermined inverse problem is

$$\mathbf{R} = \mathbf{G}^t(\mathbf{G}\,\mathbf{G}^t)^{-1}\mathbf{G} \tag{1}$$

where $\mathbf{G}$ is the matrix of the elastic Green function [*Okada*, 1992] used in the slip distribution inversion. Figure 3a shows the diagonal of matrix $\mathbf{R}$, which represents the sensitivity of the GPS array to variations in slip at each patch on the fault. The resolution, a dimensionless quantity, varies from 1 in well-resolved areas to 0 in essentially unresolved areas. Inspection of the resolution matrix shows that the available GPS data constrain mostly the upper part of the fault. A critical value of resolution $R = 0.1$ is reached at a depth of about 7 km. Figure 3b shows off-diagonal components of the resolution matrix of equation (1) for slip patches down to 8 km depth. Resolution on deeper patches is degraded, as expected. Off-diagonal terms indicate the correlation between inferred slip on a fault patch and neighboring patches. For example, inference of slip on a fault patch intersecting the Earth's surface at along-strike position $x = 24$ km is unbiased. However, inferred slip at the ends of the fault, away from most GPS stations, is less

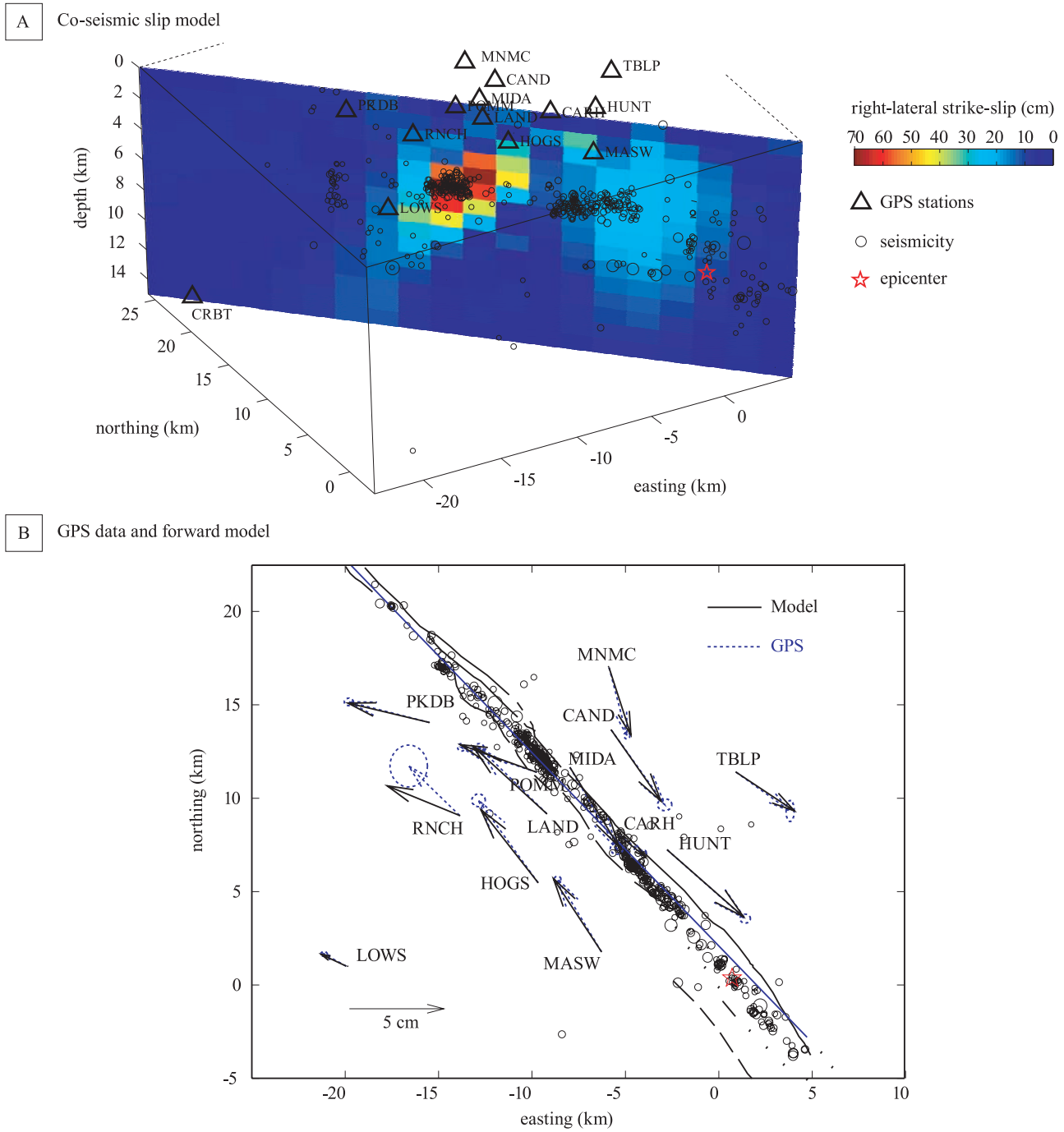

Figure 1. Coseismic slip model. (a) Amplitude of right-lateral strike slip inferred from the inversion of the 14 continuous GPS horizontal coseismic displacements. (b) Map view of the coseismic displacement vectors. The blue arrows represent the GPS data with the two-sigma uncertainties; the black arrows correspond to our best forward model. The origin is located at (N35.8150, W120.3740).

resolved. For the slip patch at depth of 5 km and along-strike position of x = 24 km, the inferred slip location is more robust along the strike than along the dip direction. At the same position in azimuth but greater depth, the inferred slip is more diffuse and azimuthal position is less robust. We conclude that inversion for slip using the current distribution of GPS stations is robust down to a depth of about 7 km immediately below the center of the GPS array at along-strike range x = 18–30 km. We note however that the inferred slip at about 5 km depth might appear distributed along a greater depth range of about 2–3 km.

[8] Our coseismic slip model exhibits two zones of relatively high slip (see Figure 1a). The area to the northwest, characterized by the highest slip, is directly below the GPS array, above the 7 km resolution limit of the array aperture, and is therefore a well-constrained feature. The second area, to the southeast and closer to the epicenter, is farther away from the GPS network and extends to a depth

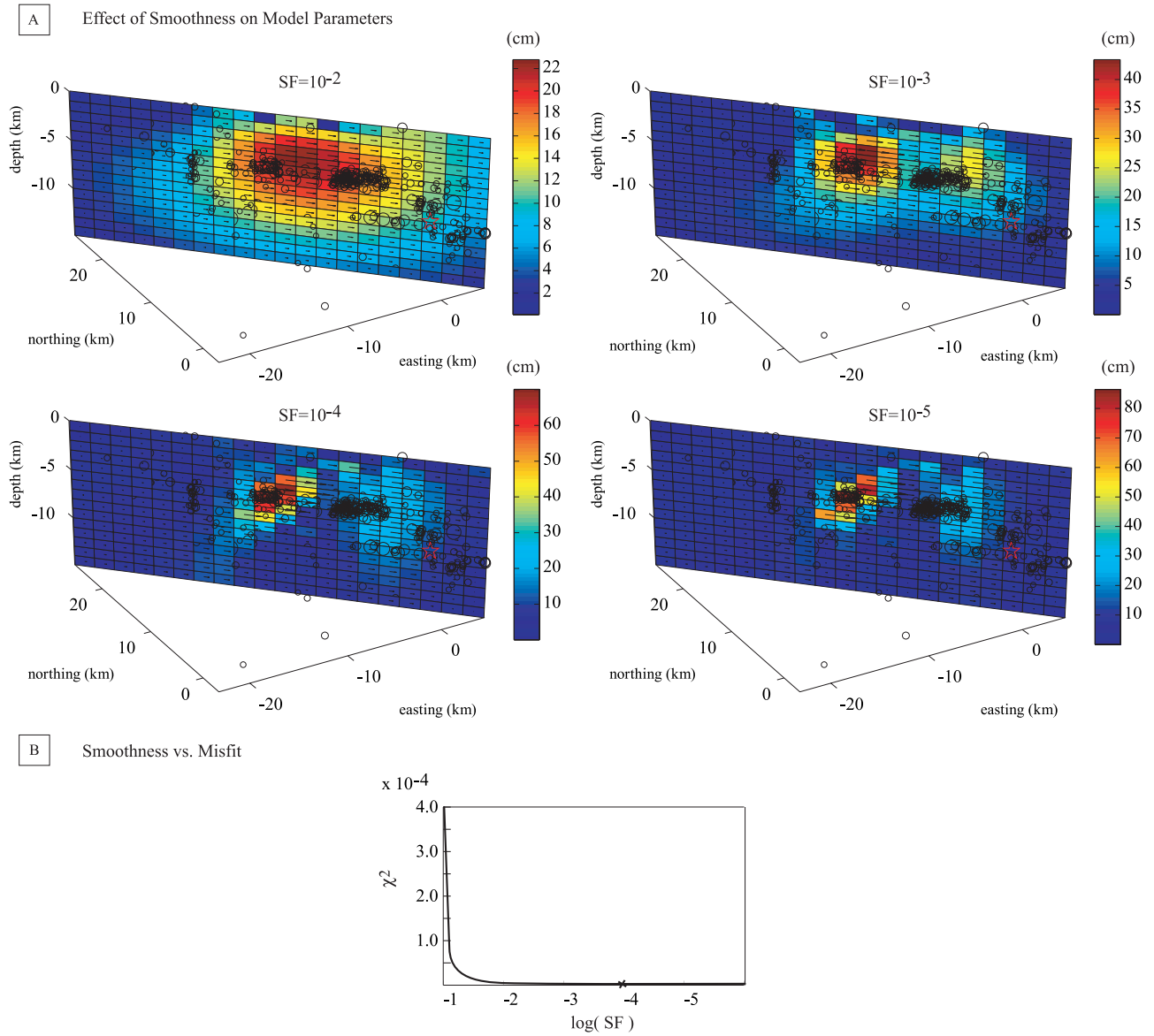

Figure 2. (a) Effect of smoothing on the coseismic slip model. The smoothness of the slip model is controlled by the smoothness factor (SF) in the inversion. (b) The smoothness/misfit curve. Our models use smoothness factor SF = 10^{-4} as indicated by the black cross.

of 10 km. The corresponding slip is more poorly constrained and might be oversmoothed.

3. Postseismic Transient Deformation

[9] Large earthquakes are usually followed by episodes of gradually decaying deformation. Various mechanisms proposed to explain the postseismic transients include poroelastic rebound [*Peltzer et al.*, 1998; *Jonssón et al.*, 2003; *Fialko*, 2004a], afterslip on the ruptured fault or its extension [*Marone et al.*, 1991; *Savage et al.*, 1994; *Fialko*, 2004b; *Freed et al.*, 2006; *Barbot et al.*, 2008b], and viscoelastic relaxation in the lower crust or upper mantle [*Nur and Mavko*, 1974; *Pollitz et al.*, 2000; *Freed and Bürgmann*, 2004]. Several authors have shown that the postseismic transient following the 2004 Parkfield earthquake is dominated by afterslip [e.g., *Johnson et al.*, 2006; *Johanson et al.*, 2006; *Freed*, 2007]. The focus of this study is the physical mechanisms of afterslip caused by the 2004 event. We utilize the network of 14 continuous GPS stations [*Langbein and Bock*, 2004] to infer a time-dependent postseismic slip on the fault plane. We use SOPAC's filtered daily position time series where a common mode noise has been removed. The methodology for noise reduction is standard, and details are given by *Wdowinski et al.* [1997]. We isolate the postseismic signal from the filtered GPS time series by removing a linear trend corresponding to the interseismic displacements. The time window used in the regression for interseismic velocities corresponds to the interval from first availability of data to December 2003, before the occurrence of neighboring San Simeon earthquake. The duration of the time series used in the inversion at each GPS station varies from 2.2 to 7.2 years and is listed in Table 1. Inferred interseismic GPS velocities and uncer-

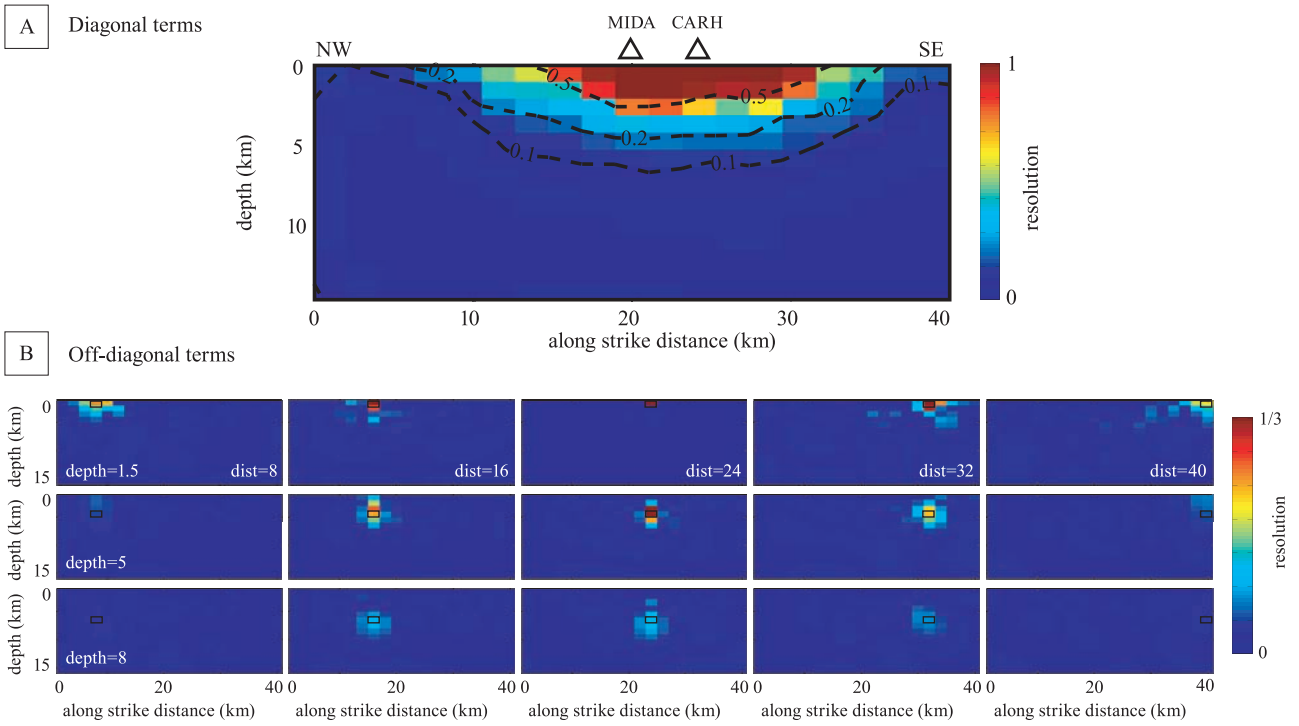

Figure 3. Resolution of the underdetermined inverse problem. (a) Diagonal of the resolution matrix **R**. Critical value $R = 0.1$ is reached at a depth of about 7 km. (b) Correlation of inferred slip patches with their neighbors on the fault plane (off-diagonal terms of the resolution matrix). Position of central subpatches is indicated in white text (depth and distance along strike) and highlighted by black rectangle. Note the change of color scale in Figure 3b. The fault segment that experienced the most afterslip is located at an along-strike distance of 24 km and a depth of 5 km; its location is robust in the strike direction.

tainties are shown in Table 1. We also remove the coseismic displacements due to the December 2003 M_w 6.6 San Simeon and the 2004 Parkfield earthquakes, along with other spurious static offsets. (Some static offsets appear in GPS time series after antenna updates.) Postseismic data clearly show that the transient deformation triggered by the coseismic stress change is still occurring 3 years after the earthquake (see Figures 7 and 10).

[10] We invert the postseismic signal for cumulative afterslip as a function of time. Formalism of the inversion is the same as the one used for the coseismic model discussed above (including the smoothing constraint and the resolution, as shown in Figure 3). Most of the surface displacements occur during the first year following the earthquake. Figure 4 shows snapshots of the inferred afterslip evolution at 0.05, 0.15, 0.30, 0.70, 1.10, 1.50, and 2.50 years after the main event. We did not regularize the afterslip evolution in the time domain which may result in spurious variations in slip velocity (e.g., see a patch of high slip at along-strike distance of 30 km at time 0.7 year that disappears at later times, Figure 4). Such second-order variations in the inferred cumulative afterslip are likely due to unmodeled periodic signals and the presence of noise in the postseismic time series [*Williams et al.*, 2004; *Langbein*, 2008]. GPS horizontal displacements and fit to the data are shown in Figure 5. Most stations are very well fitted by our afterslip models throughout the 3 year interval. Given that the 2004 Parkfield earthquake induced little if any viscous relaxation in the lower crust or upper mantle [*Johnson et al.*, 2006; *Freed*, 2007], our results confirm that the postseismic deformation is primarily driven by right-lateral afterslip on the fault plane. Station CARH, located inside the fault zone, exhibits a reversal in the direction of motion. This behavior is likely due to slip migration to a nearby parallel fault strand [*Murray and Langbein*, 2006].

Table 1. Inferred Velocity of the SCIGN Continuous GPS Stations Before the December 2003 San Simeon Earthquake[a]

Name	Lon	Lat	t (years)	V_N (m/a)	V_E (m/a)	σ_N (mm/a)	σ_E (mm/a)
CAND	−120.433	35.939	4.3	−0.0242	0.0070	0.1	0.1
CARH	−120.430	35.888	2.3	−0.0353	0.0159	0.2	0.2
CRBT	−120.750	35.791	2.2	−0.0380	0.0211	0.3	0.3
HOGS	−120.479	35.866	2.3	−0.0348	0.0175	0.2	0.2
HUNT	−120.402	35.880	2.3	−0.0274	0.0082	0.1	0.1
LAND	−120.473	35.899	4.3	−0.0346	0.0173	0.2	0.1
LOWS	−120.594	35.828	2.3	−0.0365	0.0200	0.2	0.1
MASW	−120.443	35.832	2.3	−0.0348	0.0168	0.2	0.1
MIDA	−120.458	35.921	4.3	−0.0236	0.0085	0.2	0.2
MNMC	−120.434	35.969	2.3	−0.0239	0.0055	0.2	0.2
PKDB	−120.541	35.945	7.2	−0.0351	0.0188	0.1	0.1
POMM	−120.478	35.919	4.3	−0.0343	0.0161	0.2	0.2
TBLP	−120.360	35.917	2.3	−0.0255	0.0039	0.2	0.5
RNCH	−120.524	35.899	2.2	−0.0375	0.0167	0.7	0.8

[a]Time t refers to the duration of the interval used for the linear regression. Parameters V_N, V_E, σ_N and σ_E are the north and east components of the GPS velocity and corresponding standard deviation, respectively.

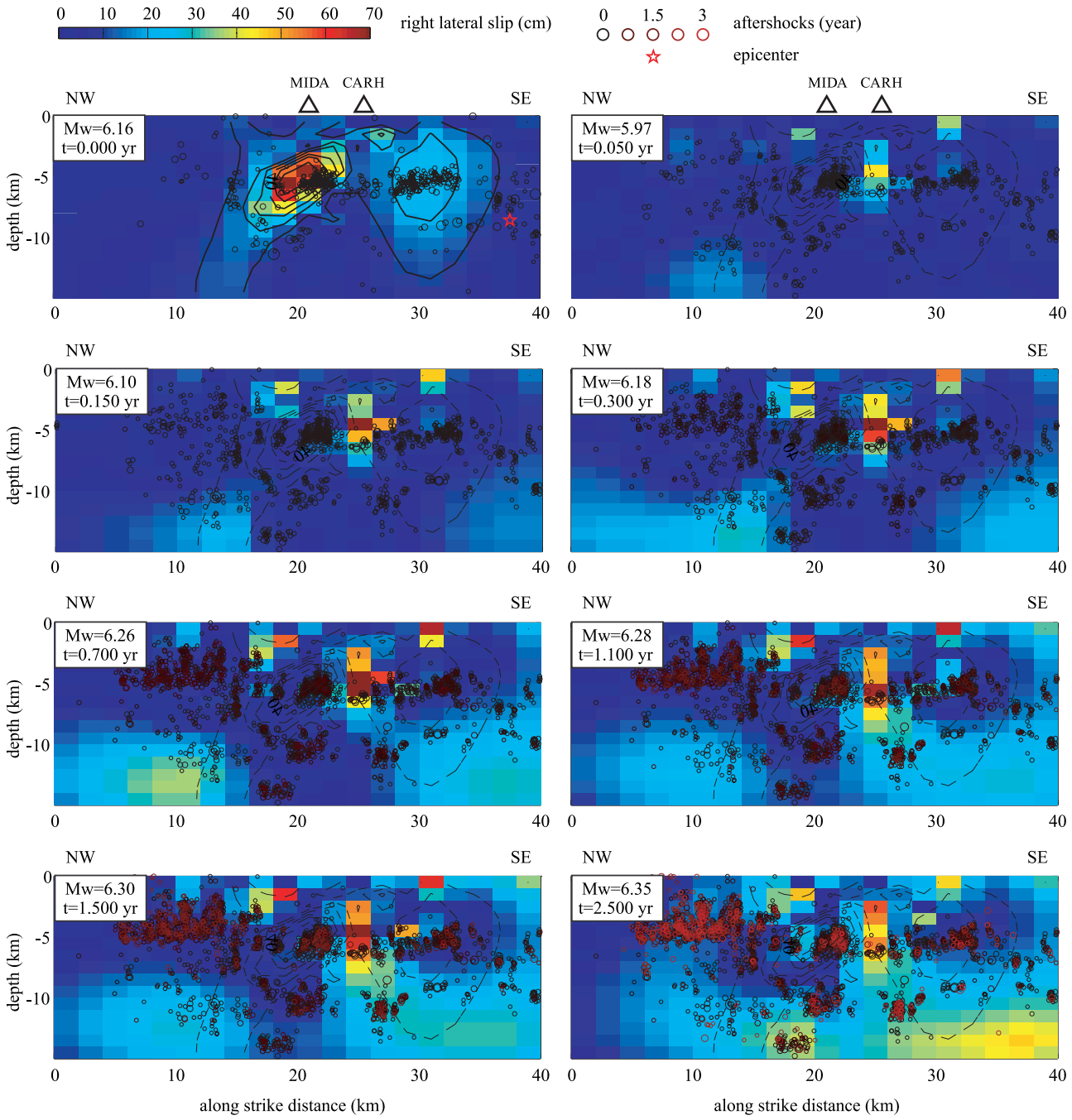

Figure 4. Kinematic inversions and seismicity. The right-lateral slip on the fault plane as a function of time after the coseismic rupture is constrained from the continuous GPS data. The $t = 0.000$ year model is the coseismic slip distribution along with the 1 day seismicity. The continuous profiles are the coseismic slip contour intervals. The cumulative afterslip models at 0.05, 0.15, 0.30, 0.70, 1.10, 1.50, and 2.50 years after the earthquake are also shown. Aftershocks, cumulative since the day following the earthquake, are superimposed to the afterslip models, colored from black to red for early to late occurrence time. The coseismic contour lines are superimposed to the afterslip models to facilitate comparison.

[11] Also shown in Figure 4 is our coseismic slip model (for $t = 0.000$ year) and the cumulative seismicity. The coseismic slip contour lines are superimposed on all kinematic inversions to facilitate comparison between coseismic and postseismic slip distributions. At early stages of deformation, afterslip occurs principally around a depth of 5 km, between two areas of high coseismic slip. In the time interval of about 3 months, afterslip reaches an equivalent geodetic moment greater than the seismic moment of the Parkfield earthquake, in agreement with earlier results by *Johanson et al.* [2006]. After 2.5 years, afterslip reaches a cumulative geodetic moment of M_w 6.35 (c.f. our inferred coseismic moment of M_w 6.16). The shallow location (depth smaller than 7 km) of early afterslip is robust, given the

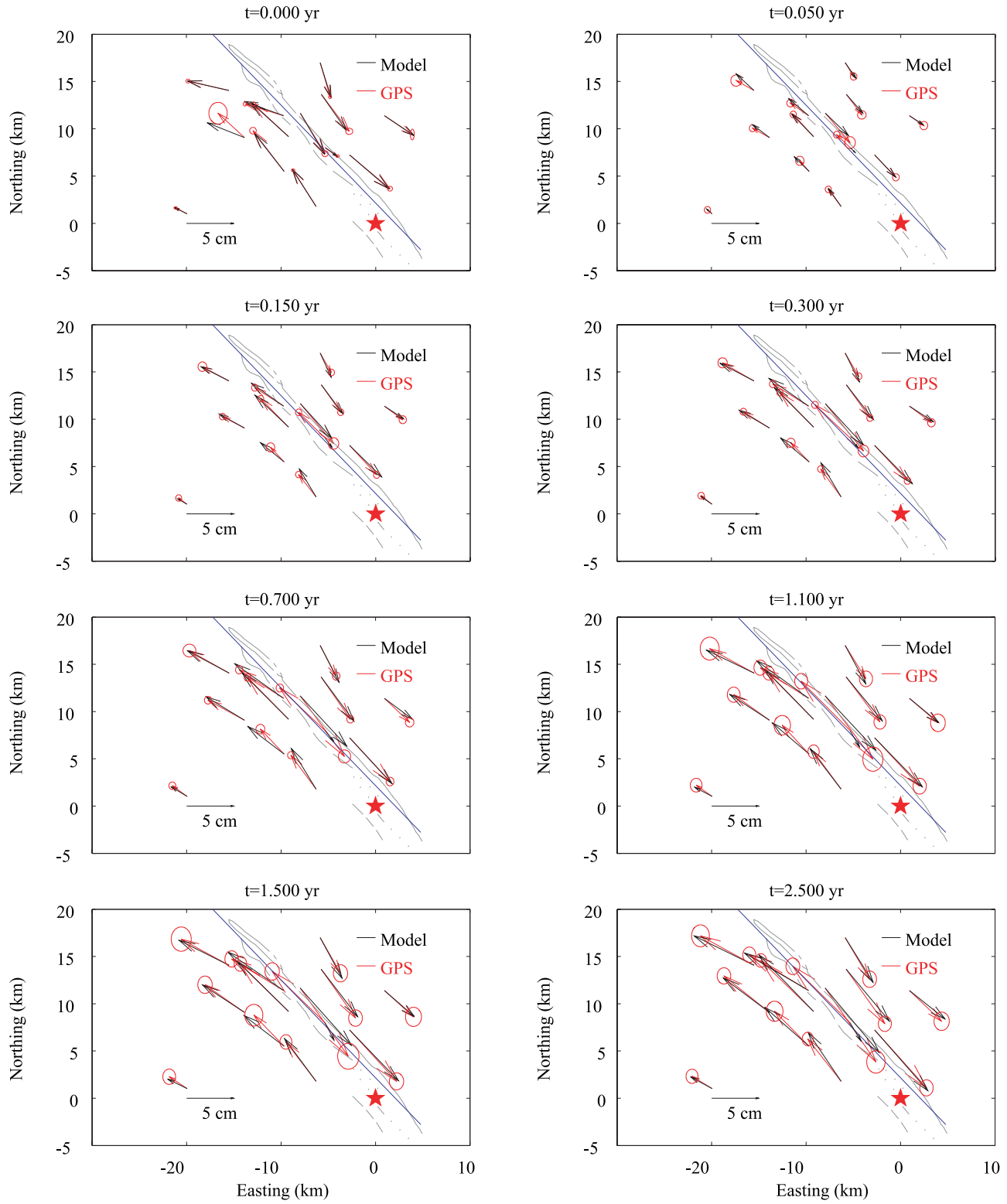

Figure 5. Kinematic inversions (continued). GPS horizontal displacements (red arrows with two-sigma uncertainties) and corresponding forward models (black arrows). The GPS data in the 3 year postseismic transient can be explained by right-lateral afterslip on the coseismically ruptured fault segment. Origin is at the geographic coordinate (N35.8150, W120.3740).

sensitivity of the GPS array (Figure 3). We performed two other series of inversions of coseismic and postseismic GPS data varying the discretization of the fault plane as a function of depth [*Fialko*, 2004a; *Fialko et al.*, 2005]. In these inversions we increased the along-strike and the downdip dimensions of subfault rectangles by 25% and 50%, respectively, resulting in a sampling of the deepest part of the fault by 5 to 4 slip patches, respectively. We find

that, similar to what appears in Figure 4, coseismic slip and afterslip occupy a remarkably complementary area on the fault plane. There is no resolvable overlap between afterslip and coseismic slip. At later times, some afterslip occurs also at greater depth, but the location cannot be precisely inferred from the available data. Our estimate of the postseismic geodetic moment includes the poorly resolved deep slip (Figure 3) that occurs in the last 2 years and may be biased toward higher values in this period. Earthquake locations correlate with areas of coseismic slip and seem not to evolve spatially throughout the postseismic epoch. Afterslip is confined to areas of low seismicity and does not represent deformation due to aftershocks.

[12] Time-dependent kinematic inversions of GPS data suggest that afterslip occurs at the periphery of the coseismic rupture, in areas characterized by low aftershock activity. Such aseismic creep is suggestive of spatial variations in frictional properties on the San Andreas fault near Parkfield. In particular, velocity-weakening areas appear to correspond to zones of high seismicity and coseismic slip; velocity-strengthening areas appear to pose an obstacle to rupture propagation and to the occurrence of aftershocks, but favor postseismic creep.

4. Models of Time-Dependent Deformation

[13] We investigate several mechanisms that might contribute to the observed deformation pattern. The deformation may be localized on a frictional surface [*Marone et al.*, 1991; *Marone*, 1998; *Scholz*, 2002] or in a ductile shear zone [*Evans and Kohlstedt*, 1995; *Roberts and Turcotte*, 2000; *Montési*, 2004]. In the latter case, the so-called plastic instabilities can spread over a narrow, yet finite, volume encompassing the fault zone. In case of a frictional interface, all deformation is accommodated by slip on a narrow fault. These two hypotheses give rise to specific constitutive laws relating the effective stress to the slip rate.

[14] Shear failure and slip at seismogenic depth are controlled by the Coulomb stress [*Byerlee*, 1978], which is to the first order given by

$$\tau - \mu\sigma = 0 \tag{2}$$

where τ is the amplitude of shear stress in the direction of sliding, σ is the effective normal stress accounting for the pore pressure contribution (positive for compression) and μ is the coefficient of friction. We decompose shear and effective normal stresses resolved on a fault into a background (e.g., tectonic) level and a coseismic change, respectively,

$$\begin{aligned} \tau &= \tau_b + \Delta\tau \\ \sigma &= \sigma_b + \Delta\sigma \end{aligned} \tag{3}$$

In the context of strike-slip faulting, we further assume that the change in the normal stress is negligible compared to the tectonic and lithostatic contributions

$$\Delta\sigma \ll \sigma_b \tag{4}$$

and that the preearthquake Coulomb stress is negligible compared to the coseismic stress change,

$$\Delta\tau \gg \tau_b - \mu_0\sigma_b \tag{5}$$

Under these assumptions, the effective stress driving afterslip on the fault plane is the shear component of coseismic loading $\Delta\tau$. Subsequent evolution of stress changes depends upon a particular mechanism of shear.

[15] Plastic instabilities can be modeled with linear or power law creep rheologies [*Weertman and Weertman*, 1964, 1975; *Evans and Kohlstedt*, 1995]:

$$\dot{\gamma} = A\left(\frac{\Delta\tau}{G}\right)^n \tag{6}$$

where $\dot{\gamma}$ is the rate of plastic strain, n is a power exponent between 1 and 5 indicating the degree of stress sensitivity, G is the shear modulus, and A is the reference strain rate controlling the timescale of deformation. For $n = 1$, the creep rheology is linear and $\eta = G/A$ is the viscosity. Equation (6) may be coupled to thermal softening, which implies depth-dependent parameters [*Kohlstedt et al.*, 1995]. Dependence on thermal or other specific state parameters can simply be included by allowing parameter A to vary spatially.

[16] Localized slip on frictional interfaces can be described by rate- and state-dependent friction laws [*Ruina*, 1983; *Dieterich*, 1992]

$$\mu = \mu_0 + a\ln\left(\frac{\dot{s}}{\dot{s}_0}\right) + b\ln\theta \tag{7}$$

where $\dot{s}$ is the slip rate on the fault, μ_0 is the coefficient of friction at a reference slip rate $\dot{s}_0$, a and b are the frictional parameters and θ is a state variable subjected to an evolution law. Under the consistency condition (2) and the assumptions (4) and (5), the friction law can be written

$$\dot{s} = \dot{s}_0\theta^{-(b/a)}e^{\Delta\tau/a\sigma} \tag{8}$$

where the ratio b/a is a work-hardening parameter, weakening for $b/a > 1$ and strengthening for $b/a < 1$. An unphysical feature of the original rate-and-state formulation (7) is an asymptotic divergence of friction at small velocities $\dot{s} < \dot{s}_0$. We adopt a generalized version of equation (7),

$$\mu = \mu_0 + a\sinh^{-1}\left[\frac{\dot{s}}{2\,\dot{s}_0}\,\theta^{b/a}\right] \tag{9}$$

motivated by thermodynamic considerations [*Lapusta et al.*, 2000; *Rice et al.*, 2001]. Under the same assumptions the corresponding slip rate is

$$\dot{s} = 2\,\dot{s}_0\theta^{-(b/a)}\,\sinh\Delta\frac{\tau}{a\,\sigma} \tag{10}$$

Note that formulations (7) and (9) or, equivalently, formulations (8) and (10), are asymptotically equivalent at high velocities, but equations (9) and (10) remain bounded at small slip rates. We assume that most of the postseismic

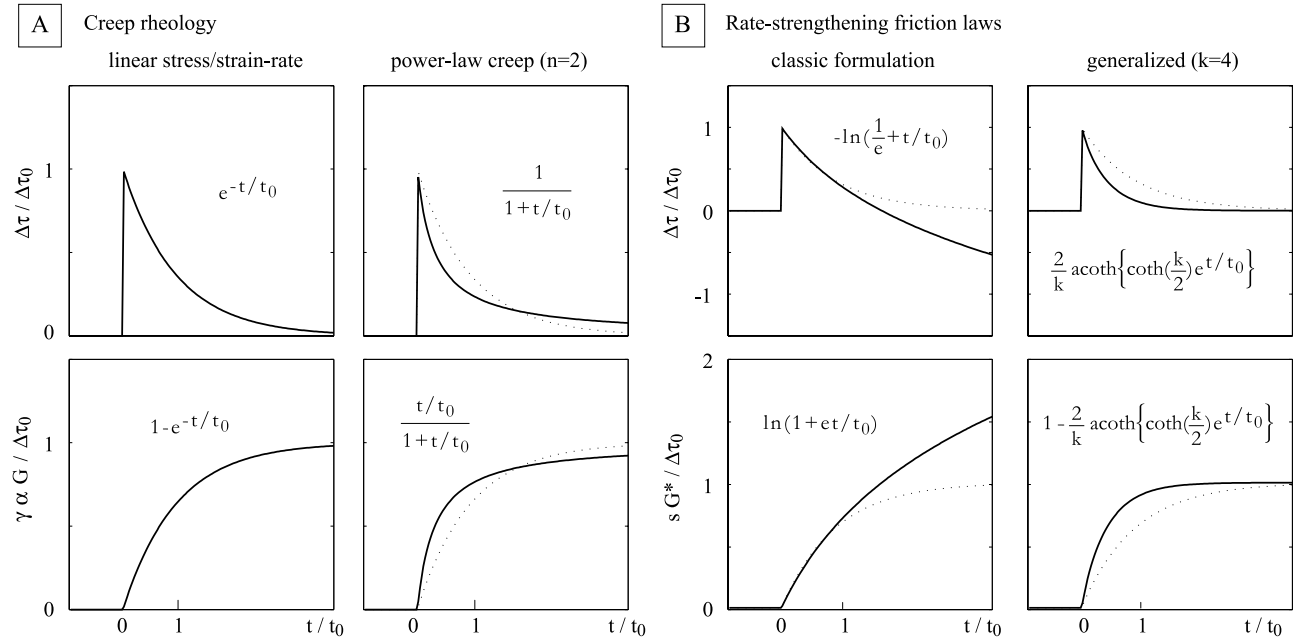

Figure 6. Creep tests for a simple crack frictional surface. The stress and strain impulse responses for (a) the linear and power law creep and (b) the rate-strengthening (RS) friction laws. For a step-like increase in total strain, resulting from an instantaneous change in stress $\Delta\tau$, some inelastic deformation is triggered. The dotted profiles indicate the response of a linear rheology. The classic formulation of RS friction is ill-posed for a creep test, whereas the generalized friction law remains bounded at small velocities. The detail of calculations can be found in Appendix A.

creep occurs at steady state ($\dot{\theta} = 0$) and we ignore the healing and slip-weakening effects. The steady state assumption is valid only if the cumulative afterslip largely exceeds the strengthening or weakening distance D_c of the state variable. The magnitude of afterslip at Parkfield reaches about half a meter (see Figure 4), which is several orders of magnitude larger than values of D_c inferred from laboratory experiments [*Marone*, 1998]. The steady state assumption gives rise to a purely rate-strengthening constitutive law

$$\dot{s} = 2\,\dot{s}_0 \sinh\left[\frac{\Delta\tau}{a\sigma}\right] \tag{11}$$

which represents the direct effect between slip rate and stress change. Note that formulation (11) resembles the empirical relationship of *Garofalo* [1975] for power law breakdown [*Tsenn and Carter*, 1987]. Velocity-strengthening friction models are an approximation to the full rate- and state-dependent friction model for a positive parameter $(a - b)$ and negligible evolution of the state variable, $\dot{\theta} = 0$ [e.g., *Marone et al.*, 1991; *Marone*, 1998; *Perfettini and Avouac*, 2007]. We note that the rate-strengthening (RS) friction parameter $\dot{s}_0$ does not correspond to the so-called ''interseismic'' velocity of the friction interface (see discussion in Appendix C). Equation (11) relates the rate of steady afterslip to coseismic stress change, and RS parameter $\dot{s}_0$ is a rock property that controls the timescale of transient slip episodes similar to parameter A in power law models.

[17] To test the predictive power of RS friction and power law creep in explaining the GPS time series, we consider the impulse response of a simple shear zone. For a planar shear crack, afterslip is controlled by the effective stiffness of the slip patch

$$G^* = \frac{C\,G}{L} \tag{12}$$

where scalar C is a dimensionless constant close to 1 that depends on the geometry [*Eshelby*, 1957; *Kanamori and Anderson*, 1975; *Shearer*, 1999; *Fialko*, 2007] and L is the linear dimension of the crack. The strain accumulated across a ductile shear band of linear dimension L and thickness T depends upon its aspect ratio $\alpha = CT/L$. Figure 6 illustrates the impulse response to an instantaneous stress change for the linear and power law creep rheologies, as well as for the classic and generalized rate-strengthening laws. Details of calculations are given in Appendix A. The impulse response for a linear rheology is

$$\gamma(t) = \frac{\Delta\tau_0}{\alpha G}\left(1 - e^{-t/t_0}\right) \tag{13}$$

where γ is the strain across the ductile shear zone, $\Delta\tau_0$ is the initial shear traction, t_0 is the relaxation timescale. A schematic of the creep evolution described by equation (13) is shown in Figure 6a (left) and superimposed on other profiles as a dashed line. Linear creep is a particular case of power law creep for the case $n = 1$ (see equation (6)), and of the generalized rate-strengthening friction for large $a\sigma/\Delta\tau_0$. The power law response

$$\gamma(t) = \frac{\Delta\tau_0}{\alpha G}\left(1 - \left[1 + \frac{t}{t_0}\right]^{(-1)/(n-1)}\right), \quad n > 1 \tag{14}$$

associated with the timescale

$$t_0 = \frac{1}{A\,(n-1)} \left(\frac{G}{\Delta\tau_0}\right)^{n-1} \tag{15}$$

is illustrated in Figure 6 for a power exponent $n = 2$. Compared to the linear case most of the deformation happens at an early time but complete relaxation, however, takes a much longer time. In case of rate-strengthening friction, the dimensionless ratio

$$k = \frac{\Delta\tau_0}{a\,\sigma} \tag{16}$$

controls the degree of nonlinearity during slip evolution, similar to the exponent n for power law creep. The impulse response of strain for RS friction is

$$s(t) = \frac{\Delta\tau_0}{G^*}\left[1 - \frac{2}{k}\coth^{-1}\left(e^{t/t_0}\,\coth\frac{k}{2}\right)\right] \tag{17}$$

where we defined the reference time

$$t_0 = \frac{1}{2\,\dot{s}_0}\,\frac{a\,\sigma}{G^*} \tag{18}$$

Deformation is also characterized by high velocities at early times, but reaches complete relaxation more rapidly, compared to linear or power law models. Note that strain rates predicted by equation (17) eventually vanish, as stress is relaxed, in contrast to the prediction of the original form of rate-dependent friction, shown in Figure 6b (left).

[18] We test whether the impulse response of power law creep and the generalized rate-strengthening friction law are able to explain the observed GPS time series. We use solutions (13), (14), and (17) for the deformation of a simple crack to fit the GPS time series. We optimize the timescale t_0, an amplitude and a nonlinear coefficient (parameters n or k for power law and RS friction, respectively) to reduce a misfit between the data, with associated uncertainties, and the forward models. Inversions are performed with a random walk and simulated annealing with a positivity constraint on model parameters [e.g., *Tarantola*, 2004]. We first performed a series of inversion of individual time series. We found that, regardless of the rheology considered, inferred model parameters were remarkably consistent among GPS stations and components. The uniformity of inferred timescale t_0 and nonlinear coefficient is indicative of a time-space separable source mechanism.

[19] Motivated by this finding, we perform a Principal Component Analysis (PCA) of the GPS time series [*Dong et al.*, 2006]. Considering that individual time series are ordered as lines in matrix $\mathbf{X}$, we define the projection $\mathbf{Y} = \mathbf{P}^T\mathbf{X}$, with $\mathbf{P}^{-1} = \mathbf{P}^T$, such that

$$\begin{aligned}\mathbf{\Lambda} &= \mathrm{Cov}(\mathbf{Y}) \\ &= \mathbf{P}^T\mathrm{Cov}(\mathbf{X})\mathbf{P}\end{aligned} \tag{19}$$

where $\mathbf{\Lambda}$ is the diagonal covariance matrix of the PCA modes. As one has

$$\mathbf{X} = \mathbf{P}\mathbf{Y} \tag{20}$$

the original time series can be decomposed into a linear combination of the PCA modes [*Menke*, 1984; *Preisendorfer and Mobley*, 1988]. Matrix $\mathbf{Y}$ is an orthogonal basis of $\mathbf{X}$ because the individual times series that occupy lines of $\mathbf{Y}$ have no correlation (in other words, Cov ($\mathbf{Y}$) is diagonal). We obtain the PCA decomposition of GPS time series by applying the spectral decomposition of the covariance matrix of $\mathbf{X}$. The eigenvalues correspond to the variance of individual modes in base $\mathbf{Y}$. Eigenvalues and eigenvectors $\mathbf{\Lambda}$ and $\mathbf{P}$ are arbitrarily scaled. We normalize them consistently so that the dominant mode eventually reaches 1 at the end of the time series. As eigenvectors are a linear combination of the original GPS signals, we obtain uncertainties on $\mathbf{Y}$ by a simple error propagation method. At first approximation, uncertainties on individual modes are reduced by a factor of $\sqrt{2N}$, where N is the number of GPS stations. Figure 7 shows the first and second most dominant modes. The decomposition consists of a time series and a spatial distribution. The signal with most variance explains 95.2% of the data. The time-dependent signal corresponds to a postseismic transient and associated vector displacements are consistent with right lateral motion on the fault. We performed a kinematic inversion for fault slip using the spatial distribution of displacement of the first mode shown in Figure 7 (top right). The slip distribution is dominated by a small slip patch centered at 5 km depth similar to the last slip distribution in Figure 4. The second mode is due to a common mode seasonal signal, which is not removed from the SOPAC filtered time series [*Langbein*, 2008] and is about 2 orders of magnitude smaller. The associated GPS displacements appear to be generally perpendicular to the fault. We consider the first mode to be representative of the postseismic response.

[20] We test the possibility of the impulse response of different rheologies to explain the dominant PCA mode. We use a random walk with simulated annealing to find the amplitude C, timescale t_0 and nonlinear coefficient (n or k) required by the data. In a series of inversions we impose the degree of nonlinearity to illustrate its role in reducing the data. Results are shown in Table 2. We compute the square root of the weighted sum of the square of the residuals for the first two months and for the entire duration of the time series. These are reported in Table 2 as χ_1 and χ_2, respectively. As we normalized the first PCA mode to reach the value of 1 after 3 years, the inferred amplitude C of fit functions is an indicator of the degree of completion predicted by the different models. For example, values of $C \simeq 1$ indicate a postseismic transient close to termination whereas higher values indicate an ongoing transient. For both power law and RS friction rheologies, the residuals are reduced by increasing the degree of nonlinearity. The best model for power law corresponds to $n = 6.9$, associated with an amplitude of $C = 2.03$. The best power law model predicts that the post-Parkfield transient is only half complete. The best RS friction fit to the PCA mode is superior to those of power law models, as shown by the short-term and the long-term residual norms. The best fit is obtained for $k = 7.0$ and $C = 1.25$, indicating that the afterslip is only 75% complete 3 years after the earthquake. The better fit of the RS model favors the rate-strengthening creep model over the power law shear zone model.

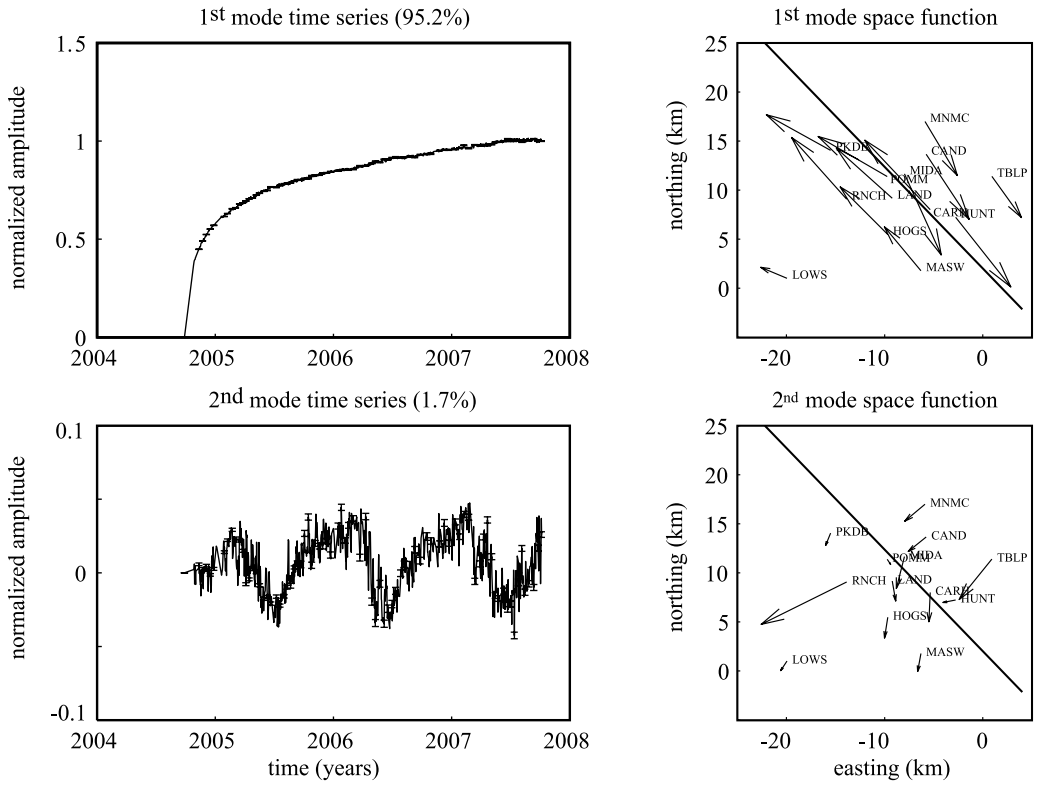

Figure 7. PCA decomposition of GPS time series. The first mode, with 95% of the total variance, corresponds to the postseismic signal. The associated GPS displacements exhibit the expected signature of right-lateral slip on the fault and correspond to the cumulated surface displacement after 3 years. The second mode, which represents 1.7% of the total variance, is due to a common mode seasonal signal, which is not removed from the SOPAC-filtered time series [*Langbein*, 2008], and is about 2 orders of magnitude smaller. The associated surface displacements are generally aligned perpendicular to the fault.

[21] The excellent fit of the RS friction model to the observed time series lends support to our assumptions (4) and (5). The best power law creep model gives rise to an inferior fit with a power exponent outside of the experimentally measured range [*Weertman and Weertman*, 1964, 1975; *Tsenn and Carter*, 1987; *Kohlstedt et al.*, 1995; *Montési and Hirth*, 2003], and we conclude that the bulk of postseismic relaxation is due to afterslip governed by a generalized rate-strengthening friction model. All original time series are well explained by equation (17) for values of k ranging from $k = 5$ to $k = 8$. Best fit for the first PCA mode is obtained, as shown in Figure 8 and Table 2, for $k = 7$. Inferred magnitude of the corresponding timescale is subject to greater uncertainty, with $t_0 = 4.8 \pm 2.4$ years.

[22] As evidenced by our geodetic inversions (Figure 4), the afterslip occurring in the first 4 months following the Parkfield earthquake is located between two patches of high coseismic slip, at about 5 km depth, in an area having a characteristic radius $l = 2$ km. In the first 4 month period, the equivalent geodetic moment due to afterslip, assuming $G = 30$ GPa, reaches 2.1×10^{18}N (equivalent M_w 6.18), compared to a cumulative seismic moment of aftershocks of 8.2×10^{14}N (M_w 3.9) over the same time period in the top 10 km. The lack of coseismic slip and the occurrence of essentially aseismic afterslip are interpreted as indicating the presence of a velocity-strengthening area in the middle of a nominally velocity-weakening layer at depth of 5 km.

[23] As postseismic creep gives rise to a total slip of $s \simeq 0.5$ m, an estimate of the effective stress drop is [e.g., *Eshelby*, 1957; *Kanamori and Anderson*, 1975; *Shearer*, 1999; *Fialko*, 2007]

$$\Delta\tau_0 = C\frac{s}{l}G \simeq 2.5 \times 10^{-4} G \tag{21}$$

where G is the shear modulus of the upper crust and C is a constant, of order of unity, that depends upon the geometry

Table 2. Best Fitting Parameters to the First Mode of the PCA Decomposition[a]

Rheology	C	t_0	n or k	χ_1	χ_2
Power law	0.93	2.8	1	4.1×10^{-1}	7.6×10^{-2}
	1.04	0.23	2	2.4×10^{-1}	4.2×10^{-2}
	1.19	0.10	3	1.7×10^{-1}	3.0×10^{-2}
	2.03	0.03	6.9	8.1×10^{-2}	1.6×10^{-2}
RS	0.93	0.38	1	3.9×10^{-1}	7.2×10^{-2}
	0.94	0.47	2	3.4×10^{-1}	6.2×10^{-2}
	0.99	0.9	4	1.7×10^{-1}	3.2×10^{-2}
	1.25	4.8	7.0	3.2×10^{-2}	1.0×10^{-2}

[a]The time series is fitted with the functional describing the impulse response of power law creep and rate-strengthening (RS) friction. Fit parameters C, t_0, and n or k are the amplitude, the timescale, and the nonlinear exponent (n for power law and k for RS), respectively, estimated from the inversion. Misfits χ_1 and χ_2 measure the residual variance for the first two months and for the 3 years time series, respectively.

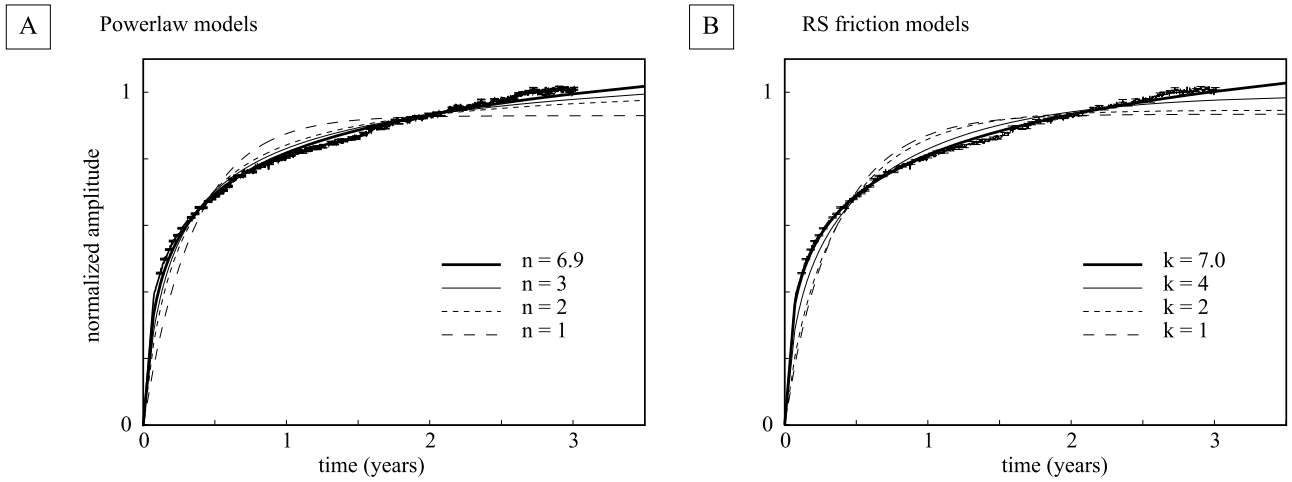

Figure 8. Functional fit to the dominant PCA mode of the postseismic component of the GPS time series. The impulse response of linear constitutive laws ($n = 1$ for power law or $k \simeq 1$ for RS friction, shown by long-dashed profiles) only poorly simulate the observed time dependence of afterslip. (a) Best fitting power law and (b) RS models, corresponding to parameters $n = 6.9$ and $k = 7.0$, respectively, are represented by the thick solid lines. In other inversions, nonlinear coefficient n or k are imposed.

of the slip patch. Static values of the shear modulus are not well constrained, but likely vary between 3 and 30 GPa, leading to estimates of the stress drop between $\Delta\tau_0 = 0.75$ MPa and $\Delta\tau_0 = 7.5$ MPa. For a uniform rock density of $\rho = 2700$ kg/m^3, the lithostatic pressure at 5 km depth is $p = 135$ MPa. Using our inference of $k = 7$, a low-end shear modulus, and assuming an effective normal stress of $\sigma = 100$ MPa, our low-end estimate of the frictional parameter is

$$a = \frac{\Delta\tau_0}{k\,\sigma} \simeq 10^{-3} \tag{22}$$

Considering the range of possible values of the shear modulus, estimate of the friction parameter can vary between $a \simeq 10^{-3}$ and $a \simeq 10^{-2}$. Noting that parameter a is a proxy for $(a - b)$ in the context of full rate- and state-dependent friction, our inferred value falls in the range of frictional parameters observed in laboratory experiments, with values for $(a - b)$ lower than 10^{-2} at temperatures corresponding to the middle of the seismogenic zone [*Scholz*, 1990, 1998; *Marone*, 1998]. Using the same assumptions, the timescale inferred from fitting the GPS data gives rise to

$$\dot{s}_0 = \frac{\Delta\tau_0}{2\,G^*\,t_0} \simeq 5 \times 10^{-5}\,\mathrm{m\,a^{-1}} \tag{23}$$

The Maxwell relaxation time t_m associated with afterslip on a simple crack depends upon the effective crack stiffness,

$$t_m = \frac{\Delta\tau}{G^*\dot{s}} \tag{24}$$

The inferred value for the RS parameter $\dot{s}_0$ corresponds to linear relaxation timescales growing from $t_m = 0.45$ year, at onset of transient deformation, to $t_m \simeq 200$ years at later times. Estimates of the velocity parameter based on GPS time series and analytic solutions for a point source might be biased by a spatially variable afterslip on the fault. The effective timescale of deformation might be longer than that for a point source, and therefore equation (23) should be considered a lower bound. We conclude that the parameters obtained from fitting equation (17) to the postseismic GPS signal are consistent with a physical model of stress relaxation. The better fit of the RS model within a reasonable range of parameters contrasts with the inferior fit obtained with a power law model that requires an exponent inconsistent with the laboratory data. Notice that the 3 year time series corresponding to the 14 GPS stations can be explained with a model having only 3 degrees of freedom. Another approach to explain the data, relating surface displacements to rate of aftershocks [e.g., *Savage et al.*, 2007], requires many more degrees of freedom.

[24] The inferred rate-strengthening segment of the fault experiencing an accelerated creep after the 2004 Parkfield earthquake is estimated to be slipping at rates of 1.1 mm/a in the interseismic period in response to slip at 33 mm/a below the seismogenic zone [*Murray et al.*, 2001], on the downdip extension of the San Andreas fault (see Appendix C). However, a shallow rate-strengthening patch was not apparent in inferred slip distributions corresponding to the interseismic period [*Murray et al.*, 2001; *Murray and Langbein*, 2006]. The surface velocities in GPS network corresponding to this shallow creep patch alone vary between 0.01 mm/a at the closest station and 0.001 mm/a at the furthest station. Such small surface velocity contributions are below the detection limit, given GPS uncertainties and the rate of interseismic loading of 33 mm/a at the bottom of the seismogenic layer.

5. Semianalytic Models of Afterslip

[25] As our analysis of the GPS data using solutions for a simple crack impulse response (section 4) favored the

generalized friction model, we further explore the latter using full 4-D simulations with a finite source. We model the aseismic creep occurring after the Parkfield event using a semianalytical model of deformation in an viscoelasto-plastic half-space. Our approach allows one to evaluate a time-dependent deformation due to a quasi-static fault slip in response to the driving coseismic stress changes. Our model includes the linear and power law creep as well as the generalized velocity-strengthening friction law, but on the basis of the results in section 4, we focus on RS models. We compute deformation due to fault creep using integral transforms [*Barbot et al.*, 2008a]. The time-dependent fault creep is modeled by integrating the constitutive laws with a second-order accurate Runge-Kutta method with adaptive time steps. Details of our modeling approach and example calculations are discussed in Appendix B.

[26] We evaluate the velocity-strengthening parameters using our coseismic slip model as the initial condition driving the afterslip sequence. Guided by results of kinematic inversions (Figure 4), we assume that areas of high coseismic slip are velocity weakening and do not participate in postseismic creep. We also assume that areas on the periphery of high-slip asperities are predominantly velocity strengthening. Because seismic slip may have propagated into a transition between the velocity-weakening and velocity-strengthening areas, we include this zone in our model by limiting the coseismic slip distribution to areas where coseismic slip was greater than 0.2 m (about 30% of maximum coseismic slip). We compensate the reduction in geodetic moment by rescaling the amplitude of the coseismic slip model. The result is a more compact slip distribution where the two main coseismic slip patches are separated by a RS patch that did not slip during the 2004 earthquake. The coseismic slip model is shown in Figure 4 by the contours. The rest of the fault is allowed to participate in afterslip driven by the coseismic stress changes. We do not constrain the rake of afterslip. The slip direction is dictated by the instantaneous stress field (and may in general have a dip-slip component).

[27] We compute displacements resulting from time-dependent creep on a fault plane at the location of the 14 GPS stations. To evaluate how well the generalized rate-strengthening model is able to explain the GPS data, we perform a grid search to find the coefficient $a\sigma$ that best explains the postseismic time series. In each numerical solution, we fit the GPS signals to find the reference strain rate $\dot{s}_0$ that gives rise to the largest misfit reduction at all stations.

[28] Figure 9 shows snapshots of the simulated RS creep evolution on the fault plane. Afterslip takes place in the middle of the two patches of high coseismic slip and propagates preferentially toward the free surface. At later times our model predicts more shallow afterslip than is actually deduced in kinematic inversions. We suggest that this difference may result from the assumption of uniform frictional parameters on the fault plane. A higher value of $\dot{s}_0$ near the surface would delay the occurrence of shallow afterslip. Investigations of the depth dependence of frictional properties is beyond the scope of the study. Figure 10 shows the GPS displacements and our best fitting model. For each forward model associated with a value of $a\sigma$, one parameter, $\dot{s}_0$, controlling the timescale of deformation, is optimized through a grid search. Amplitude of displacements at each station is determined from the elastic Green function. Stations CARH and MIDA, in the very near field, are the only GPS stations showing a large misfit. This misfit may be due to our assumption of afterslip occurring on a geometrically simple fault plane. At the rest of the stations, our model predicts the correct sense of horizontal displacements, and most forward models are within the uncertainties of GPS measurements (95% confidence interval). Despite the approximations introduced in the initial condition, the forward model results in more than 70% variance reduction.

[29] We computed a series of solutions for different values of $a\sigma$ ranging from 0.2 MPa to 1.4 MPa, assuming a shear modulus of $G = 30$ GPa, and inverted GPS data for the reference slip rate $\dot{s}_0$. Variables $\dot{s}_0$ and a in our formulation correspond to the parameter V_0 and the steady state friction parameter $(a - b)$, respectively, in spring-slider analogs of rate- and state-dependent friction [e.g., *Dieterich*, 1994; *Marone et al.*, 1991; *Marone*, 1998; *Perfettini and Avouac*, 2007]. Figure 11 shows the misfit and inferred velocity V_0 as a function of the velocity-strengthening parameter $(a - b)$, assuming an effective normal stress $\sigma = 100$ MPa. We evaluated the misfit between data and model during the first year of deformation (dashed profiles) and the entire 3 years of data. Variance reduction is slightly better for the shorter interval, but in general is quite consistent. For both periods, we obtain the best fit for $(a - b) = 7 \times 10^{-3}$ and $\dot{s}_0 = 20$ mm/a. Smaller values of $(a - b)$ give rise to a higher misfit, but the variance reduction remains sufficiently low for higher values of $(a - b)$. Our finite size source modeling essentially provides a lower bound on the frictional parameter $(a - b)$.

[30] Inferences of RS parameter $(a - b)$ in our full 3-D calculation are not biased by a particular choice of the shear modulus in the homogeneous elastic half-space. Some bias in estimating steady state friction parameters may arise due to the presence of a compliant fault zone [*Fialko et al.*, 2002; *Fialko*, 2004b; *Hamiel and Fialko*, 2007; *Barbot et al.*, 2008a, 2009]. As we model the Parkfield coseismic rupture and the subsequent creep using the same value for the rigidity, corresponding to the compliant zone, this potential bias is limited. Another bias may come from using daily GPS solutions to derive the coseismic model, which might map some early afterslip into the coseismic model. We ignore the evolution of the state parameter. For this reason, we expect our forward models to be less accurate in the first few days following the rupture and to capture accurately the longer timescale deformation. Parameters inferred from 3-D calculations are consistent with our impulse response estimates in section 4, and our preferred value of $(a - b) = 7 \times 10^{-3}$, corresponding to the largest misfit reduction, is at the high end of inferences from laboratory experiments [*Marone*, 1998].

6. Discussion

[31] The 2004 M_w 6.0 Parkfield earthquake triggered a transient deformation that was responsible for larger cumulative surface displacements compared to those from the main event. Velocities that are higher than the interseismic

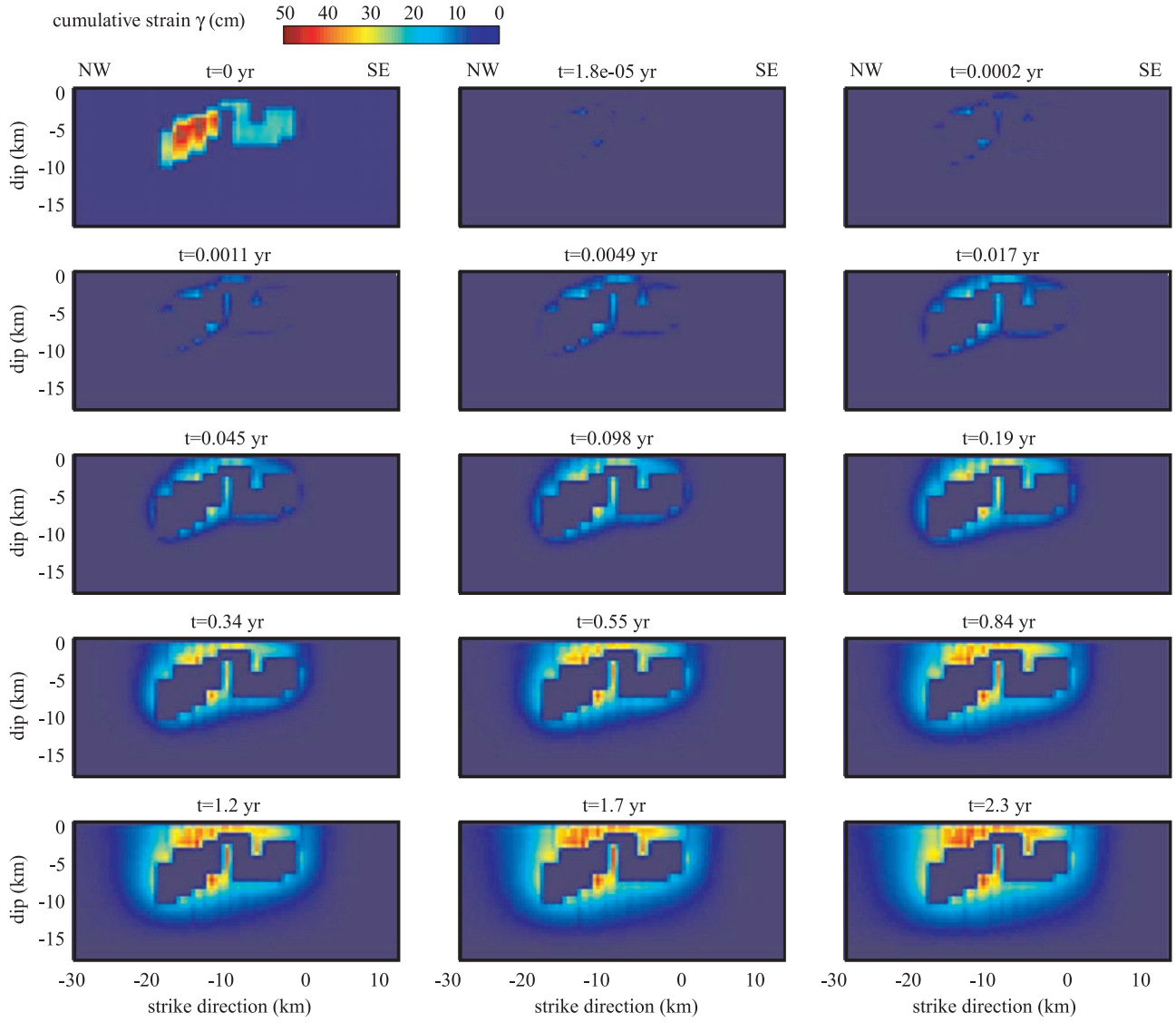

Figure 9. Numerical simulation of afterslip with rate-strengthening (RS) friction. The simplified coseismic model (t = 0 plot) is the initial condition for the postseismic fault creep. Time evolution of afterslip is described by the generalized RS friction law of equation (11). Afterslip is not allowed to occur in areas that slipped coseismically and propagates on the fault plane away from the coseismic patch. The corresponding time series of surface displacements are shown in Figure 10. Snapshots are separated by 20 time steps. The numerical method is described in Appendix B.

ones are still observed at near-field GPS stations 3 years after the event. Our inversions of the continuous GPS postseismic time series reveal that afterslip occurred conspicuously between two areas of high coseismic slip at depth of about 5 km, in the middle of the seismogenic zone. Numerous aftershocks following the earthquake are located mostly in areas that participated in seismic slip, and not in areas that hosted postseismic creep. We conclude that the post-Parkfield transient deformation is due to aseismic slip that relaxed the stress increase caused by the main shock. Furthermore, observations of microseismicity and aftershocks of previous Parkfield earthquakes have shown that earthquakes occur repeatedly on the same asperities, suggestive of variations in effective frictional properties on the fault plane [*Waldhauser et al.*, 2004]. Our time series analysis and finite source modeling of the GPS data indicate that afterslip occurred on a periphery of patches of high seismic slip, and is likely governed by a rate-strengthening friction law.

[32] Results of our modeling bear on the extrapolation of laboratory measurements to natural faults. Our inferred value of the steady rate-strengthening frictional parameter is of order of $(a - b) = 7 \times 10^{-3}$. Typical laboratory measurements at temperatures representative of the seismogenic zone suggest values of the friction rate parameter in the range from 0 to 0.006, depending on the cumulative shear displacement experienced by the samples [*Marone*, 1998; *Scholz*, 2002]. *Morrow and Lockner* [2001] found the velocity dependence of friction $(a - b) = 0.005–0.007$ for samples of the Hayward fault for a variety of rocks in effective pressure conditions simulating depths of burial up to 12 km. Experiments with clay minerals in pressure

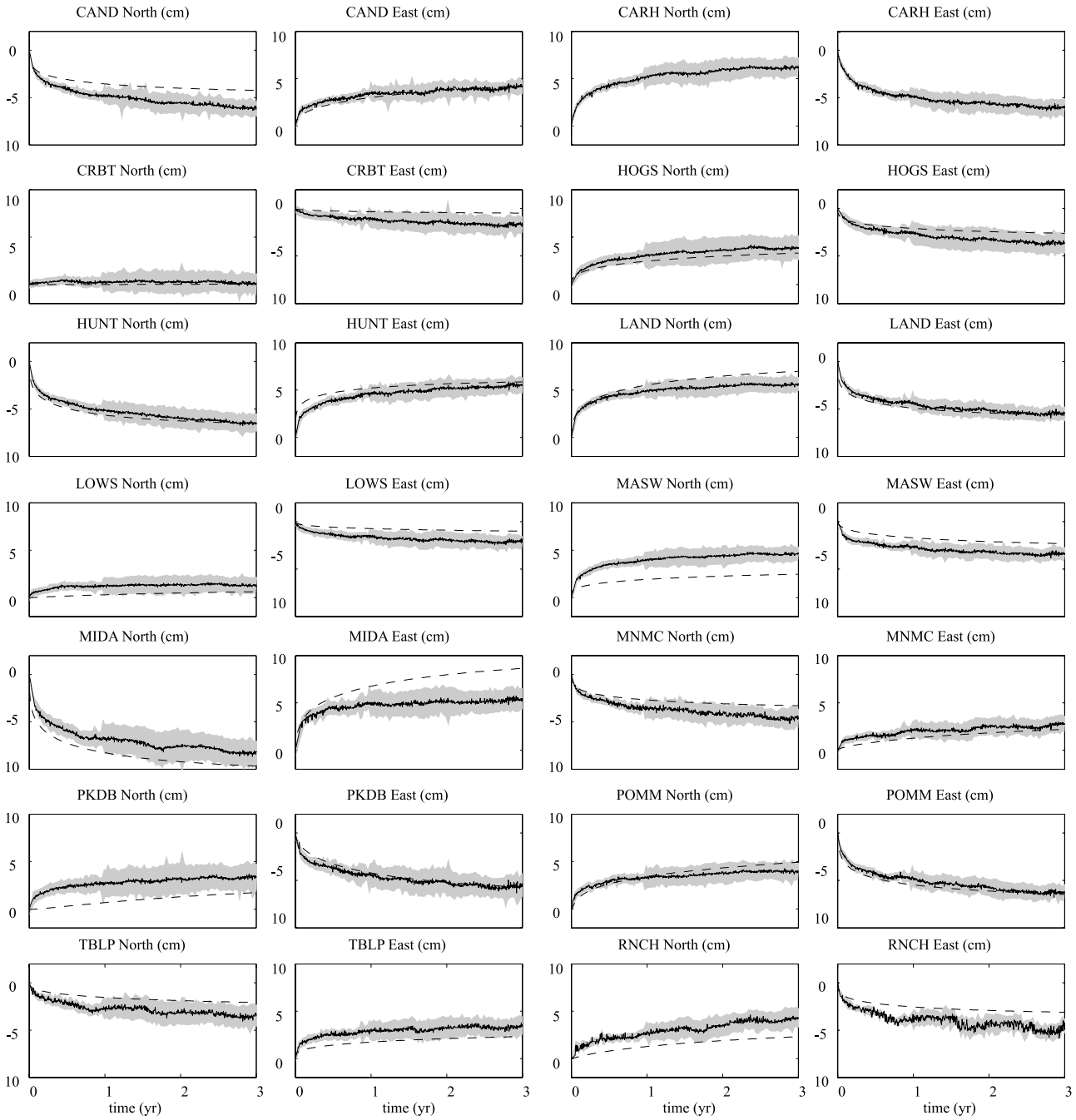

Figure 10. Postseismic GPS data (solid line), two-sigma uncertainties (gray shade), and best forward model (dashed lines) corresponding to the generalized rate-strengthening friction law for all the continuous GPS stations. Model prediction generally agrees with the data with the exception of station CARH and MIDA, in the very near field, which are affected by a fault migration.

conditions relevant to the top 15 km revealed a rate-strengthening friction with parameter $a - b = 0.007$ [*Morrow et al.*, 1992]. Experiments on thick gouge layers sheared between rough surfaces at high normal stress [*Marone et al.*, 1990] predict higher friction rate parameters, and seem to be most consistent with our inferences of $(a - b)$ on a mature fault such as the San Andreas fault in the Parkfield area.

[33] *Johnson et al.* [2006] modeled the afterslip evolution following the 2004 Parkfield event using a full rate- and state-dependent friction formulation. In their approach afterslip is controlled by the preearthquake stress level on the fault, the stress change due to the earthquake and frictional properties on the fault (a, b, critical slip distance D_c and V_0), some of which are allowed to vary laterally and with depth. They invert for a range of parameters that reproduces the GPS 9 month time series. They find a rate-strengthening coefficient of $(a - b) = 10^{-4} - 10^{-3}$, an order magnitude lower than values inferred from laboratory experiments. In our study, we use longer (3 years) time series and constrain

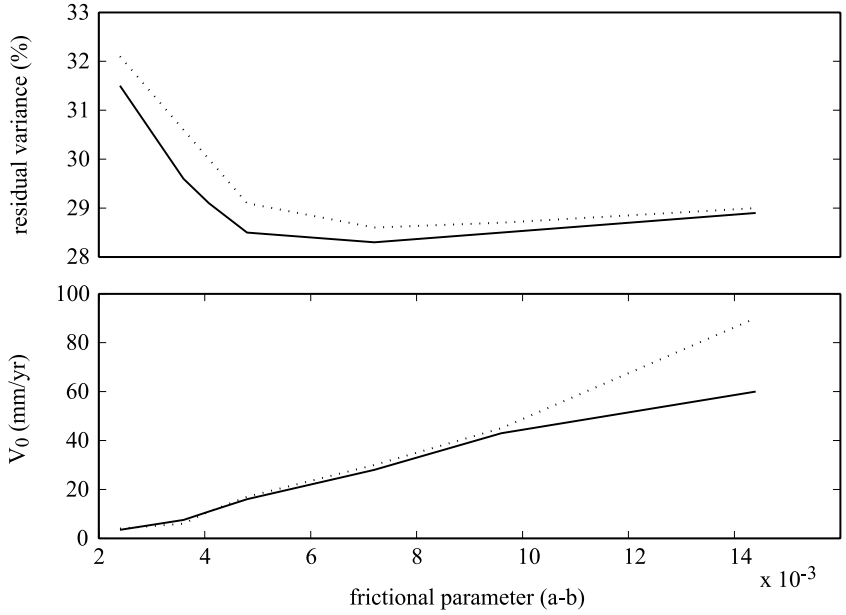

Figure 11. Constraint on frictional parameters V_0 and $(a - b)$. The velocity best reducing the data for the 13 selected stations (CARH is removed) is inverted using only 1 year of data (dashed profiles) and 3 years of data (solid lines). Results are shown for a series of $(a - b)$ models, assuming an effective normal stress of σ = 100 MPa.

the fault frictional properties with (1) time series analysis and (2) a pure rate-strengthening model with lateral variations in frictional properties. Our kinematic inversions of afterslip show that much of postseismic slip occurs on a patch between seismic asperities so we model a fault with uniform frictional properties that we attribute to this slipping patch. Our best afterslip model explains 70% of the 3 year GPS signal and produces fit to the data that is comparable to that of *Johnson et al.* [2006] (see Figure 11) over the first 9 months. A reasonably good performance of our simpler model compared to the approach of *Johnson et al.* [2006] can be explained by the fact that most of afterslip occurs in a limited area and samples the frictional properties of the fault at this location.

[34] The aftershock sequence following the 2004 Parkfield earthquake has a cumulative moment much lower than the geodetic moment due to postseismic creep. The equivalent geodetic moment for afterslip, assuming a shear modulus of G = 30 GPa, exceeds 3.23×10^{18} N (M_w 6.3) 3 years after the earthquake whereas aftershocks account for a moment of 5.96×10^{16} N (M_w 5.15) in the same period. The higher moment of afterslip compared to cumulative moment of aftershocks disfavors the assumption that postseismic creep is driven by the occurrence of aftershocks [*Savage and Yu*, 2007]. The depth distribution of aftershocks is trimodal, as shown in Figure 12c (also, see Figure 4). Most earthquakes occur between 3 and 9 km depth, with cumulative magnitude of M_w 4.26. The rest of the moment release is due to three large aftershocks that occurred at greater depth (>10 km). The moment release due to shallow (depth <10 km) aftershocks is found to be strongly correlated with aseismic slip. Figure 12a shows the cumulative moment of aftershocks occurring above 9 km depth and the equivalent geodetic moment of creep estimated from our finite source modeling and the geodetic inversions. The geodetic moment corresponding to our best forward model is represented with the black solid line, assuming a shear modulus of G = 30 GPa. The geodetic moment inferred from afterslip kinematic inversions is plotted as circles. Finally, cumulative aftershock moment is shown by the dashed line. We did not remove a seismic moment rate corresponding to background seismicity from the cumulative aftershock moment. The moment of seismic noise in interseismic times is immediately overshadowed by the occurrence of larger magnitude aftershocks. Correlation between creep and seismicity seems to start 4 days (10^{-2} year) after the main shock. However, precise evaluation of the kinetics of early creep in our model is limited by our assumption of a pure rate-strengthening friction. In a rate- and state-dependent friction model, the state variable accounts for the effect of fault contact aging on the effective friction. For the same stress initial condition, the initial velocity is reduced compared to a pure rate-strengthening model. As a result, the onset of excitation of aftershocks by creep could happen earlier than our model predicts. Figure 12b illustrates the relationship between the cumulative aftershock moment and estimates of the equivalent geodetic moment for the aseismic slip based on geodetic inversions and finite source forward modeling. As creep accounts for a moment release that is 2 orders of magnitude greater than that due to aftershocks, data suggest that stressing from aseismic slip in velocity-strengthening areas governs the seismicity rates in neighboring velocity-weakening areas.

[35] Similar inferences were made in previous studies of postseismic deformation in other locations, including the 1992 Landers, California [*Perfettini and Avouac*, 2007] and the 2005 Nias-Simeulue, Sumatra [*Hsu et al.*, 2006] earth-

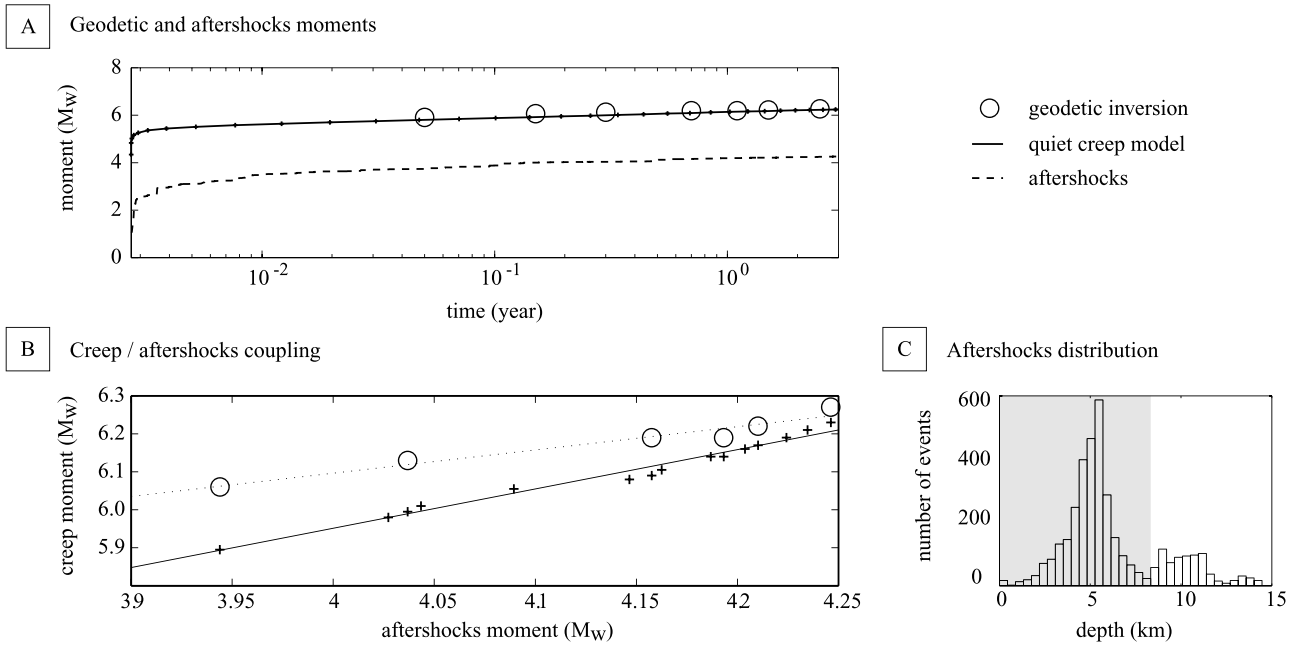

Figure 12. Aftershocks driven by aseismic creep. (a) The equivalent seismic moment of our preferred RS creep model (solid line) compares well with the equivalent seismic moment inferred from kinematic inversions (circles). Aftershocks moment (dashed line) is 2 orders of magnitude lower and follows the creep evolution closely after 10^{-2} year (4 days). (b) Linear correlation between the moment magnitudes of aftershocks and RS creep from two independent estimates of creep moment using geodetic inversion (circles) and forward modeling (crosses). The lines are a linear fit to the points. (c) Depth distribution of aftershocks. Moments in Figures 12a and 12b use the aftershocks that occurred in the top 9 km (shaded depths).

quakes. *Savage and Yu* [2007] also showed that the rate of aftershocks and surface velocities were linearly related during the first year of the postseismic transient. At Parkfield, aftershocks and afterslip occur principally at depth of about 5 km, in areas well resolved by the GPS network. The aftershocks hypocenters do not overlap with inferred areas of postseismic creep. An integrated view on seismic and aseismic transients following the Parkfield earthquake (Figure 4) suggests the presence of along-strike variations in frictional properties of the fault in the middle of the seismogenic zone. Such variations are likely due to proximity of the Parkfield segment of the San Andreas fault to the creeping section and might be rare in other locations, where the transition from velocity-weakening to velocity-strengthening behavior occurs primarily as a function of depth.

7. Conclusions

[36] We investigated the coseismic and postseismic deformation due to the M_w 6.0 2004 Parkfield, California, earthquake. We used daily position time series from the SCIGN network to derive our coseismic slip model. Inferred strike-slip distribution exhibits two areas of high slip, consistent with results of previous investigations. We find a geodetic coseismic moment of M_w 6.16, somewhat higher than the seismic moment of M_w 6.0. We next inverted the horizontal components of the postseismic time series for evolution of afterslip. Most of the postseismic data can be explained by right-lateral afterslip on the fault plane that ruptured coseismically. After 2 years, the cumulative postseismic geodetic moment reaches an equivalent magnitude M_w 6.35, higher than our coseismic geodetic estimate of M_w 6.16. During the first year following the earthquake, afterslip is confined to the upper half of the seismogenic zone, occurring principally around 5 km depth, and between two areas of large coseismic slip. There is no resolvable overlap between coseismic slip and afterslip. The aftershock sequence took place in areas devoid of afterslip, with most of the earthquakes occurring in areas that ruptured coseismically. The seismicity in the top 10 km has a cumulative moment about 2 orders of magnitude smaller than the equivalent geodetic moment of afterslip. We conclude that the postseismic transient is dominated by aseismic slip driven by coseismic stress changes and we interpret the occurrence of afterslip and aftershocks in separate locations as being due to along-strike variations in effective frictional properties.

[37] Modeling of GPS time series using solutions for shear cracks suggests that afterslip is more likely localized on discrete planes rather than distributed over finite width plastic zones with power law rheology. A rate-strengthening friction law generalized for small velocities [*Rice et al.*, 2001] can explain the surface displacements at all stages of the postseismic period. A distinction between candidate mechanisms has been possible due to availability of temporally dense GPS solutions. Power law models were found to provide an inferior fit to GPS time series. To investigate

the rate-strengthening creep hypothesis further, we developed a new semianalytic method to evaluate the time-dependent deformation due to coseismic loading in an viscoelastoplastic half-space. The method uses integral transforms to compute the three-dimensional static deformation. The time integration for a given constitutive law is performed using a second-order accurate Runge-Kutta method with adaptive time steps. We modeled the postseismic transient using the generalized rate-strengthening friction law and our coseismic slip model as initial condition. The best fitting model can explain 72% of all GPS data, except at station CARH in the very near field, which suffered a velocity reversal due to migration of the creep interface. Finite source modeling of the creep evolution puts a lower bound on the rate-strengthening frictional parameter, $a\sigma > 0.5$ MPa, in agreement with inferences from the simple crack approximation. The same rate-strengthening forward model can explain both the time dependence of GPS data and the spatiotemporal evolution of creep on the fault plane inferred from kinematic inversions.

[38] Assuming an effective normal stress of $\sigma = 100$ MPa, appropriate for 5 km depth, we infer a steady state rate-strengthening friction parameter of $(a - b) = 7 \times 10^{-3}$, which is on a high end of values measured in laboratory experiments [*Scholz*, 1990, 1998; *Marone*, 1998]. Our result suggests that laboratory data corresponding to high normal stresses and thick gauge layers are most consistent with our in situ inferences of frictional properties of mature faults such as the San Andreas fault near Parkfield. Our modeling results indicate that areas that ruptured during the 2004 Parkfield event continued to experience seismicity in the postseismic period. The occurrence of unstable sliding (stick-slip behavior), suggests that the respective areas are characterized by a negative frictional parameter $(a - b)$. The strong correlation between creep and aftershock moments, as well as the spatial anticorrelation between creep and seismicity suggest that creep is governing the rate and magnitude of aftershocks in the top 10 km of the seismogenic zone. This scenario of reloading of the velocity weakening surfaces by afterslip on nearby velocity-strengthening patches is suggestive of strong lateral variations in frictional properties along the Parkfield segment of the San Andreas fault. Velocity-strengthening areas represent an obstacle to the propagation of the main rupture and are responsible for the aseismic relaxation of coseismic stress by creep, thereafter governing the rate of seismicity in velocity-weakening areas. These results emphasize the effect of aseismic deformation on the rate of aftershocks and the spatiotemporal distribution of slip throughout the seismic cycle.

Appendix A: Impulse Response of a Point Source

[39] A finite area of localized shear with linear dimension L embedded in a elastic medium Ω with shear modulus G can be idealized with a time-space separable spring-slider model with the effective spring constant per unit area

$$G^* = \frac{C\,G}{L} \tag{A1}$$

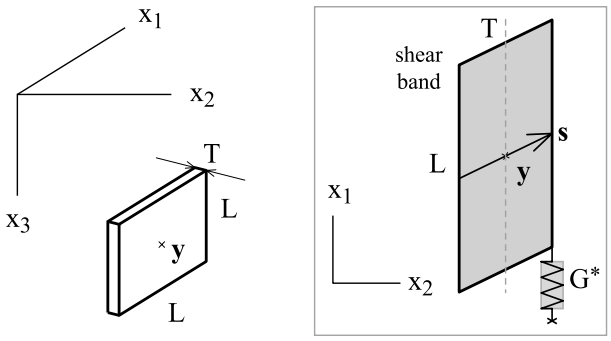

Figure A1. Schematic of the point source approximation for a localized shear band of thickness T and linear dimension L. The cumulated displacement **s** across the ductile zone relaxes the stress $\tau = G^*s$.

where scalar C is a constant close to 1 that depends on the geometry [*Eshelby*, 1957; *Kanamori and Anderson*, 1975; *Shearer*, 1999; *Fialko*, 2007]. We treat this idealization as "point source" because it ignores details of displacements within the slipped area and provides an accurate approximation in the far field. The point source approximation also assumes that stress resolved on the slip area is uniform.

[40] The inelastic response of a medium to coseismic stress change is, in general, the solution for a constant total strain $\dot{\boldsymbol{\epsilon}} = 0$ subjected to some initial conditions or, using equations (B21) and (B22), in terms of stress

$$\mathbf{D} : \dot{\boldsymbol{\sigma}} + \mathbf{F} : \boldsymbol{\sigma} = 0 \tag{A2}$$

where **D** and **F** are the elastic compliance and fluidity tensors, respectively, and $\boldsymbol{\sigma}$ is the Cauchy stress. Projecting equation (A2) in the constant strain direction **R** and using the point source approximation, we develop the associated governing ordinary differential equations for localized shear bands with power law creep and afterslip with rate-strengthening friction.

A1. Power Law Shear Bands

[41] In a simple shear zone model $s(t)$ is the displacement across the finite shear band which relaxes the stress $\tau = G^*s$. A schematic of the geometry is shown in Figure A1. The rheology of fault creep is described by equation (6) where the plastic strain rate can be approximated by $\dot{\gamma} = \dot{s}/T$, where T is the thickness of the shear zone (see Figure A1). In the case of linear creep of equation (6) with $n = 1$, the evolution of shear stress across the ductile zone is governed by the differential equation

$$\dot{\tau} + \alpha A\,\tau = 0 \tag{A3}$$

where $\alpha = CT/L$ is the aspect ratio of the ductile zone. The solution is given by

$$\tau(t) = \tau_0\, e^{-t/t_0} \tag{A4}$$

where τ_0 is the initial (coseismic) loading and the timescale

$$t_0 = \frac{1}{\alpha A} \tag{A5}$$

is independent of the initial stress condition and controlled by the aspect ratio of the ductile zone and the effective rheology of rocks within the shear zone. As stress is relaxed, cumulative displacement across the ductile volume is

$$s(t) = \frac{\tau_0}{G^*}\left(1 - e^{-\alpha A t}\right) \tag{A6}$$

Displacement in the elastic medium exhibits similar time dependence, but amplitudes decay away from the shear zone. Similarly, for nonlinear creep, the governing equation for stress on the fault plane is

$$\frac{\dot{\tau}}{G} + \alpha A \left(\frac{\tau}{G}\right)^n = 0 \tag{A7}$$

and the decay of shear stress is

$$\tau(t) = \tau_0 \left[1 + \alpha A (n-1)\left(\frac{\tau_0}{G}\right)^{n-1} t\right]^{(-1)/(n-1)} \tag{A8}$$

where the timescale of deformation t_0 scales with the reference strain rate A, the aspect ratio α and the initial stress τ_0

$$t_0 = \frac{1}{\alpha A (n-1)}\left(\frac{G}{\tau_0}\right)^{n-1} \tag{A9}$$

Integrating equations (6) and (A8), we obtain the displacement evolution across the ductile zone

$$s(t) = \frac{\tau_0}{G^*}\left[1 - \left(1 + \frac{t}{t_0}\right)^{(-1)/(n-1)}\right] \tag{A10}$$

or, in terms of strain,

$$\gamma(t) = \frac{\tau_0}{\alpha G}\left[1 - \left(1 + \frac{t}{t_0}\right)^{(-1)/(n-1)}\right] \tag{A11}$$

A2. Rate-and-State Creep

[42] For the generalized rate-strengthening friction, with a constitutive relationship represented by equation (11), the scalar ordinary differential equation for stress is

$$\frac{\dot{\tau}}{G^*} + 2\,\dot{s}_0 \sinh\left(\frac{\tau}{a\,\sigma}\right) = 0 \tag{A12}$$

where a and $\dot{s}_0$ are the frictional parameters and scalar σ is the fault normal stress (compression is assumed positive). The degree of nonlinearity in the transient sliding depends upon the dimensionless ratio

$$k = \frac{\tau_0}{a\,\sigma} \tag{A13}$$

and the resulting stress evolution on the slip patch is

$$\tau(t) = \tau_0 \frac{2}{k} \coth^{-1}\left[\exp\left(2\dot{s}_0 \frac{G^*}{a\sigma} t\right) \coth\frac{k}{2}\right] \tag{A14}$$

Introducing the timescale

$$t_0 = \frac{a\,\sigma}{2\,\dot{s}_0 G^*} \tag{A15}$$

we obtain the slip evolution

$$s(t) = \frac{\tau_0}{G^*}\left[1 - \frac{2}{k}\coth^{-1}\left(e^{t/t_0}\,\coth\frac{k}{2}\right)\right] \tag{A16}$$

The generalized friction model is highly nonlinear for $k \gg 1$, but is quasi-linear for $k \leq 1$. We note that the timescale t_0 depends upon the size of the slipping patch.

[43] Time series of postseismic deformation can be compared to predictions of equation (A6), (A11), or (A16). Inferred timescale t_0 and degree of nonlinearity (n or k in case of power law and generalized rate-strengthening friction, respectively) can be used to constrain initial effective stress and frictional parameters.

Appendix B: Numerical Model of Time-Dependent Creep on Finite Faults in an Elastic Half-Space

[44] We present a novel approach to evaluate the three-dimensional time-dependent deformation due to a localized creep in an otherwise elastic half-space. The method is based on a continuum representation of fault slip. In particular, our treatment extends the usual double-couple representation of static faults and derive an expression for the equivalent body force rate that reproduces the required slip velocity on the fault. In section B1, we introduce a formulation for slip systems that describes static slip and creeping dislocations. In section B2, we derive a continuum formulation of the constitutive and governing equations that describe afterslip of a fault plane and associated elastic deformation in a half-space. In section B3, we present details of our numerical implementation.

B1. Continuum Representation of Dislocations

[45] Faults can be viewed as dislocations that introduce an irreversible displacement discontinuity in an otherwise elastic domain. These dislocations cannot simply be treated using Dirichlet boundary conditions on each side of the interface because only the relative displacement between the two sides are formally known, as opposed to the absolute position of the particles that lie across the contact. Boundary conditions might be sensibly prescribed in terms of strain (Neumann-type boundary conditions), but a difficulty arises because of the discontinuous nature of the interface.

[46] Consider semi-infinite solid Ω with a traction-free surface $\partial\Omega$. We use a Cartesian coordinate system where position in a half-space is denoted by $\mathbf{x} = (x_1, x_2, x_3)$ with x_3 positive downward and $x_3 = 0$ at the surface $\partial\Omega$. We adopt the infinitesimal strain approximation of linear elasticity. A fault $\mathcal{S}$ is defined by a surface

$$n(\mathbf{x}) = 0 \tag{B1}$$

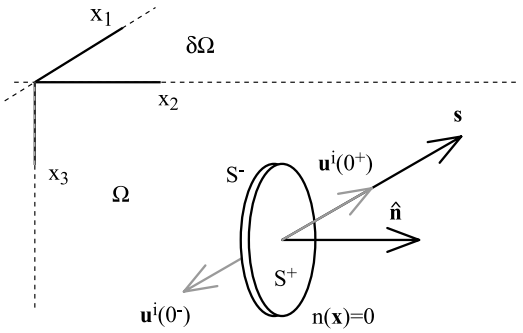

Figure B1. A buried circular slip patch embedded in semi-infinite solid Ω with free surface $\partial\Omega$ at $x_3 = 0$. Slipping surface is defined by $n(\mathbf{x}) = 0$. Burgers' vector of dislocation is $\mathbf{s} = \mathbf{u}^i(0^+) - \mathbf{u}^i(0^-)$.

The normal unit vector on $\mathcal{S}$ is the unit vector

$$\hat{\mathbf{n}} = \frac{\partial n}{\partial \mathbf{x}} \tag{B2}$$

Hereafter, we denote $\mathcal{S}^+$ one side on the fault and $\mathcal{S}^-$ the other, such as $n = 0^+$ on $\mathcal{S}^+$ and $n = 0^-$ on $\mathcal{S}^-$. After some slip occurred on the fault surface, the previously adjacent points across $\mathcal{S}$ are separated by $\mathbf{s}$, which is the Burgers' vector associated with the dislocation. We define the plastic displacement $\mathbf{u}^i(n)$, where superscript i stands for irreversible or inelastic, due to slip on the fault as follows:

$$\mathbf{u}^i(0^+) - \mathbf{u}^i(0^-) = \mathbf{s} \tag{B3}$$

A schematic of the geometry is shown in Figure B1. The gradient of the inelastic deformation is the tensor

$$\nabla \mathbf{u}^i = \frac{\partial \mathbf{u}^i}{\partial \mathbf{x}} = \hat{\mathbf{n}} \otimes \frac{\partial \mathbf{u}^i}{\partial n} \tag{B4}$$

Defining the gradient

$$\frac{\partial \mathbf{u}^i}{\partial n} = \delta(n)\, \mathbf{s} \tag{B5}$$

where $\delta(x)$ is the Dirac delta function, and integrating, we find a continuum description of plastic deformation that satisfies condition of equation (B3). Decomposing the gradient into the canonical symmetric and skew-symmetric parts

$$\nabla \mathbf{u}^i = \boldsymbol{\epsilon}^i + \boldsymbol{\Omega}^i \tag{B6}$$

respectively, we obtain the eigenstrain associated with the dislocation

$$\boldsymbol{\epsilon}^i(\mathbf{x}) = \frac{1}{2}\left(\hat{\mathbf{n}} \otimes \mathbf{s} + \mathbf{s} \otimes \hat{\mathbf{n}}\right) \delta[n(\mathbf{x})] \tag{B7}$$

The delta function of equation (B7) is a continuous representation of the fault discontinuity at $n = 0$ and also prescribes the location of the dislocation in the medium. Notice that no intrinsic fault thickness is associated with eigenstrain. In particular, eigenstrain is not defined as the ratio of some cumulative displacement over some small, yet finite, distance. The use of generalized functions to describe seismic sources has been discussed by *Backus and Mulcahy* [1976].

[47] Before completing the continuum representation of a dislocation, we consider a purely static deformation. We decompose the total strain $\boldsymbol{\epsilon}$ in the semi-infinite solid into elastic and inelastic parts

$$\boldsymbol{\epsilon} = \boldsymbol{\epsilon}^e + \boldsymbol{\epsilon}^i \tag{B8}$$

respectively, where the inelastic strain, only occurring on the dislocation, is formally valid everywhere in the solid due to the use of the Dirac delta function (equation (B7)). (In most of the domain Ω, we have $\boldsymbol{\epsilon} = \boldsymbol{\epsilon}^e$.) Using decomposition of equation (B8) the Cauchy stress becomes

$$\boldsymbol{\sigma} = \mathbf{C} : \boldsymbol{\epsilon}^e = \mathbf{C} : \boldsymbol{\epsilon} - \mathbf{C} : \boldsymbol{\epsilon}^i \tag{B9}$$

where $\mathbf{C}$ is the fourth-order elastic moduli tensor in Ω and operator : is the double scalar product. The distinction between elastic and plastic strains in the stress-strain relationship of equation (B9) makes apparent the moment density of the dislocations

$$\mathbf{m}(\mathbf{x}) = \mathbf{C} : \boldsymbol{\epsilon}^i(\mathbf{x}) \tag{B10}$$

Whereas the moment density of dislocations can be obtained by other means [e.g., *Aki and Richards*, 1980; *Shearer*, 1999], our formulation is advantageous because it includes the location, size and magnitude of the dislocations. Furthermore, using the Cauchy stress definition of equation (B9) and conservation of momentum $\nabla \cdot \boldsymbol{\sigma} = 0$, we find the inhomogeneous Navier's equation

$$\nabla \cdot (\mathbf{C} : \boldsymbol{\epsilon}) + \mathbf{f} = 0 \tag{B11}$$

where $\boldsymbol{\epsilon}$ is unknown and the body force density term is

$$\mathbf{f}(\mathbf{x}) = -\nabla \cdot \left(\mathbf{C} : \boldsymbol{\epsilon}^i(\mathbf{x})\right) \tag{B12}$$

As in the case of the moment density, the equivalent body forces for dislocations can be obtained using different approaches [e.g., *Eshelby*, 1957; *Burridge and Knopoff*, 1964]. Note that expression (B12) contains information about the double couple representation of dislocations as well as their location and size in the half-space. For example, the elastic potential energy of the dislocation is simply

$$E = \int_\Omega \boldsymbol{\sigma} : \boldsymbol{\epsilon}^i(\mathbf{x})\, dV = \int_S \boldsymbol{\sigma} : \mathbf{s} \otimes \hat{\mathbf{n}}\, dA \tag{B13}$$

which comes from the continuum representation of eigenstrain of equation (B7), the symmetry of the stress tensor and the definition of the Dirac delta function. The solution

displacement in Ω due to static slip described by equations (B7) and (B12) is

$$\begin{aligned}\mathbf{u}(\mathbf{x}) &= \int_{\Omega} \mathbf{G}(\mathbf{x},\mathbf{x}_0)\cdot\mathbf{f}(\mathbf{x}_0)\,dV \\ &= \int_{S} \nabla\mathbf{G} : \mathbf{C} : \mathbf{s}\otimes\hat{\mathbf{n}}\,dA\end{aligned} \tag{B14}$$

where $\mathbf{G}$ is the elastic Green function tensor, and last term is obtained by integration by part and using the definition of the Dirac delta function.

[48] The continuum representation of static dislocations in terms of eigenstrain accurately captures the discontinuous nature of displacement fields due to fault slip. The eigenstrain is a forcing term in the strain domain which should not be confused with the elastic strain in the near field of the dislocation. Using the tensor inner product $\langle \mathbf{A}, \mathbf{B}\rangle = \sqrt{2\mathbf{A}:\mathbf{B}}$ and assuming purely tangential fault slip (no opening or interpenetration), one can write [e.g., *Nemat-Nasser*, 2004]

$$\boldsymbol{\epsilon}^{i}(\mathbf{x}) = \gamma(\mathbf{x})\,\mathbf{R} \tag{B15}$$

where $\mathbf{R}$ is a unitary, symmetric, and deviatoric, second-order tensor and γ, the norm of $\boldsymbol{\epsilon}^{i}(\mathbf{x})$, is the total slip across the dislocation. In particular, noting $\mathbf{s} = s\hat{\mathbf{s}}$, one has

$$\gamma(\mathbf{x}) = s\,\delta[n(\mathbf{x})] \tag{B16}$$

The eigenstrain describes the slip on a fault patch. This definition can be readily extended to represent slip velocities across the dislocation. To do so, we define the eigenstrain rate

$$\dot{\boldsymbol{\epsilon}}^{i}(\mathbf{x}) = \dot{\gamma}(\mathbf{x})\,\mathbf{R} \tag{B17}$$

As shown for the case of static dislocations, the plastic deformation rate $\dot{\gamma} = \dot{s}$ nominally applies to the fault interface only but is formally valid in the entire domain Ω by use of the Dirac delta function. We use this continuum representation to formulate the constitutive equations in the solid and at the contact interface in a uniform, consistent manner. Various degrees of strain localization on a fault can be readily modeled using Dirac's delta, boxcar, Gaussian, etc., functions.

B2. Body Force Representation of Fault Creep

[49] In a general case, a static dislocation with slip vector $\mathbf{s}$ along a surface of normal $\hat{\mathbf{n}}(\mathbf{x})$ is associated with the eigenstrain

$$\boldsymbol{\epsilon}^{i} = \frac{1}{2}(\mathbf{s}\otimes\hat{\mathbf{n}} + \hat{\mathbf{n}}\otimes\mathbf{s}) \tag{B18}$$

and, in a linear elastic medium Ω with elastic tensor $\mathbf{C}$, with the moment density $\mathbf{m} = \mathbf{C}{:}\boldsymbol{\epsilon}^{i}$. The equivalent body force (formally a body force density) for such a dislocation is [e.g., *Eshelby*, 1957; *Burridge and Knopoff*, 1964; *Nemat-Nasser*, 2004]

$$\mathbf{f}(\mathbf{x}) = -\nabla\cdot(\mathbf{C} : \mathbf{s}\otimes\hat{\mathbf{n}}) \tag{B19}$$

and the resulting displacement $\mathbf{u}$ in the elastic half-space is obtained with application of the elastic Green function [*Love*, 1927; *Nemat-Nasser and Hori*, 1999]

$$\mathbf{u}(\mathbf{x}) = \int_{\Omega} \mathbf{G}(\mathbf{x},\mathbf{x}_0)\cdot\mathbf{f}(\mathbf{x}_0)\,\mathrm{d}\mathbf{x}_0 \tag{B20}$$

[50] In an viscoelastoplastic material, with elastic compliance tensor $\mathbf{D}$ and fluidity tensor $\mathbf{F}(\mathbf{x})$, the elastic strain rate tensor is

$$\dot{\boldsymbol{\epsilon}}^{e} = \mathbf{D} : \dot{\boldsymbol{\sigma}} \tag{B21}$$

and the irreversible plastic strain rate occurring on the fault is

$$\dot{\boldsymbol{\epsilon}}^{i} = \mathbf{F} : \boldsymbol{\sigma} \tag{B22}$$

where $\boldsymbol{\sigma} = \mathbf{C} : \boldsymbol{\epsilon}^{e}$ is the Cauchy stress [*Malvern*, 1969], and the amplitude of $\mathbf{F}$ is stress- and space-dependent. Note that the fluidity tensor $\mathbf{F}$ has a nonvanishing value only on the fault surface, even though it can be defined everywhere in Ω by use of generalized functions. The total strain rate is the sum of elastic and inelastic contributions

$$\dot{\boldsymbol{\epsilon}} = \dot{\boldsymbol{\epsilon}}^{e} + \dot{\boldsymbol{\epsilon}}^{i} \tag{B23}$$

Assuming infinitesimal strain, combining equations (B21), (B22), and (B23) and integrating, we obtain

$$\boldsymbol{\sigma}(t) = \mathbf{C}{:}\boldsymbol{\epsilon}(t) - \int_{0}^{t} \mathbf{C}{:}\dot{\boldsymbol{\epsilon}}^{i}(s)\,ds \tag{B24}$$

where the integrand

$$\dot{\mathbf{m}}(\mathbf{x},t) = \mathbf{C}{:}\dot{\boldsymbol{\epsilon}}^{i}(\mathbf{x},t) \tag{B25}$$

is the internal torque density applied in the solid to gradually relax stress. The total strain $\boldsymbol{\epsilon}$ can simply be evaluated from the state of current deformation

$$\boldsymbol{\epsilon}(t) = \frac{1}{2}\left[\nabla\otimes\mathbf{u} + (\nabla\otimes\mathbf{u})^{T}\right] \tag{B26}$$

We derive the solution velocities from the integration of forcing terms

$$\dot{\mathbf{f}}(\mathbf{x}) = -\nabla\cdot\left(\mathbf{C}{:}\dot{\boldsymbol{\epsilon}}^{i}\right) \tag{B27}$$

using the elastic Green function

$$\dot{\mathbf{u}}(\mathbf{x}) = \int_{\Omega} \mathbf{G}(\mathbf{x},\mathbf{x}_0)\cdot\dot{\mathbf{f}}(\mathbf{x}_0)\,\mathrm{d}\mathbf{x}_0 \tag{B28}$$

We compute the time-dependent deformation by integrating simultaneously equations (B24) and (B28).

[51] The inelastic strain rate tensor $\dot{\boldsymbol{\epsilon}}^i$ is usually decomposed into a direction $\mathbf{R}$ and a scalar strain rate $\dot{\gamma}$ [*Nemat-Nasser*, 2004]

$$\dot{\boldsymbol{\epsilon}}^i = \mathbf{F} : \boldsymbol{\sigma} = \dot{\gamma}\,\mathbf{R} \tag{B29}$$

While the decomposition (B29) is general, in the case of the extreme localization of a discontinuous fault interface the eigenstrain rate $\dot{\gamma}$ corresponds to the slip rate on the fault $\dot{\gamma} = \dot{s}$. The strain direction $\mathbf{R}$ for strike-slip and dip-slip faults is a deviatoric, symmetric and unitary second-order tensor that describes the geometry of the slip system. The traction $\mathbf{t}(\mathbf{x})$ resolved on a fault surface can be decomposed into normal and shear components,

$$\mathbf{t} = \boldsymbol{\sigma} \cdot \hat{\mathbf{n}} = (\mathbf{t} \cdot \hat{\mathbf{n}})\,\hat{\mathbf{n}} + \boldsymbol{\tau} \tag{B30}$$

Noting $\mathbf{s} = s\hat{\mathbf{s}}$, we assume that the slip rate vector is collinear with the direction of shear traction evaluated on the fault patch,

$$\dot{\mathbf{s}} = \dot{s}\,\hat{\boldsymbol{\tau}} \tag{B31}$$

Extending the static case of equation (B18) to time-dependent slip, the plastic strain rate direction becomes

$$\mathbf{R} = \frac{1}{2}(\hat{\boldsymbol{\tau}} \otimes \hat{\mathbf{n}} + \hat{\mathbf{n}} \otimes \hat{\boldsymbol{\tau}}) \tag{B32}$$

and the corresponding equivalent body force rate, from equations (B27), (B29), and (B31), simplifies to

$$\dot{\mathbf{f}}(\mathbf{x}) = -\nabla \cdot (\dot{\gamma}\mathbf{C} : \mathbf{R}) \tag{B33}$$

[52] A dislocation slips only when a yield condition $g(\boldsymbol{\sigma}) = 0$ is satisfied, such that

$$\dot{\gamma} = \begin{cases} 0, & \text{if } g(\boldsymbol{\sigma}) < 0 \\ f(\boldsymbol{\sigma}, \gamma, t), & \text{if } g(\boldsymbol{\sigma}) = 0 \end{cases} \tag{B34}$$

where in general the formulation $\dot{\gamma} = f(\boldsymbol{\sigma}, \gamma, t)$ allows for a direct effect, some work hardening and a possible healing. We use the Coulomb yield surface given by equation (2). Coseismic static displacements $\mathbf{u}(\mathbf{x}, t = 0)$ and stress change $\boldsymbol{\sigma}(\mathbf{x}, t = 0)$ define a set of initial conditions that govern the subsequent inelastic deformation. Constitutive relationships for plastic flow or generalized rate-strengthening friction, equations (6) and (11), respectively, complete the description of our model.

B3. Numerical Implementation

[53] We extend the approach of *Barbot et al.* [2008a] to three-dimensional deformation, and use integral transforms to evaluate the elastic response of a half-space, i.e., to solve equations (B20) and (B28) numerically. We perform the convolution between the equivalent body forces and the elastic Green function in the Fourier domain, taking advantage of the convolution theorem and the fast Fourier transform. The method is computationally efficient: the evaluation of the instantaneous velocity field in a 512^3 node grid with uniform sampling is obtained in a few seconds on a parallel computer with shared memory architecture. One possible drawback of Fourier methods is the periodicity of the numerical solution. We mitigate undesirable effects of periodic boundary conditions using sufficiently large computational grids. We taper the fault segments to reduce aliasing and temper stress singularities [*Barbot et al.*, 2008a]. Our approach allows one to compute deformation due to the presence of buried faults of arbitrary orientation.

[54] We benchmarked our numerical code against the analytic solution of *Okada* [1992] for strike-slip and dip-slip faults. Figure B2 shows the relative error between analytic and numerical solutions at the location of the GPS stations at Parkfield, for our inferred coseismic model. Numerical error is usually smaller than 5%, and exceeds 10% in the far field where absolute displacements are vanishingly small and at the precise location of the fault where the displacement discontinuity is represented by a continuous field. We also compared our solution to another numerical approach. Figure B2 shows the relative error introduced by the numerical Green function of *Wang et al.* [2003] for a spatial sampling of $\Delta = 0.5$ km and $\Delta = 0.2$ km. As one can see from Figure B2, our model, with a uniform sampling of $\Delta = 0.25$ km performs well compared to the method of *Wang et al.* [2003].

[55] We evaluate the integrals in equations (B28) and (B24) using a second-order accurate Runge-Kutta scheme with adaptive time steps [*Abramowitz and Stegun*, 1972]. From the instantaneous effective linear viscosity,

$$\eta(t) = \frac{\tau}{\dot{\gamma}} \tag{B35}$$

we determine the characteristic relaxation timescale

$$t_m = \frac{\eta}{G} \tag{B36}$$

where G is the shear modulus. We use a fraction of t_m, also referred to as the Maxwell relaxation time, for time increments. Finally, we estimate the spatial gradients in equation (B26) using a finite impulse response differentiator filter [*McClellan et al.*, 1973]. Filters are much better estimates of localized deformation than simple finite difference schemes because the latter smooth the derivative estimates near discontinuities such as slip on a fault.

[56] Figure B3 shows a benchmark of our approach for a simple geometry. We place a small slip patch in a coseismic stress field with a choice of parameters constrained to satisfy $t_0 = 1$ year in equations (A5) and (A9). We compare the time series of surface displacement at an arbitrary location at the surface of the half-space to the impulse response of linear and nonlinear rheologies (Figure B3b). Our adaptive time steps are apparent for the nonlinear power law creep, with shorter time increments at early time of deformation and longer ones at later times, when most stress has already been relaxed. The numerical solution is very well fit by the expected impulse response of linear or nonlinear rheologies and the theoretical timescale of deformation is recovered within a 5% error. We conclude that our modeling approach and its numerical implementation are

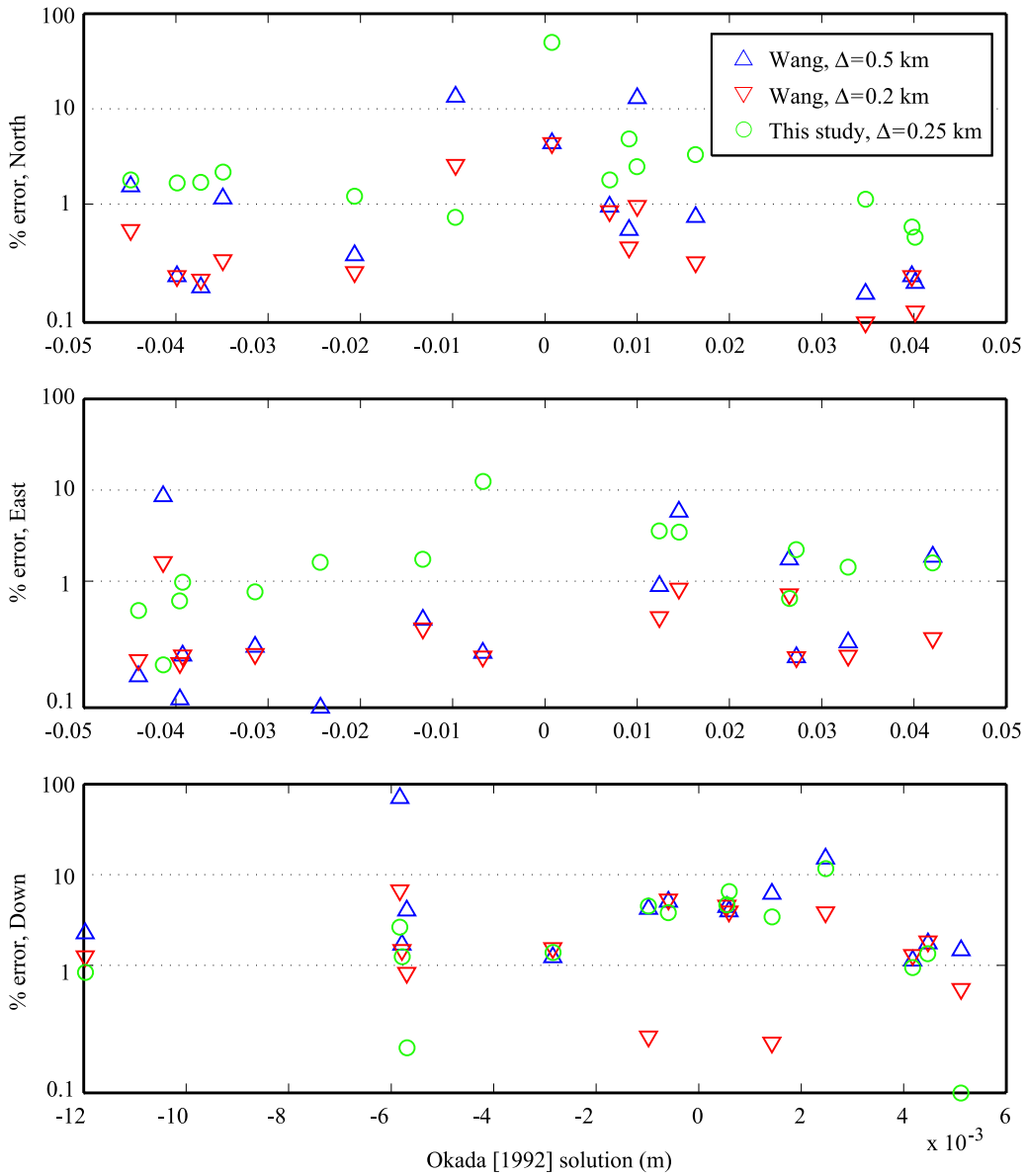

Figure B2. Relative error of numerical models compared to the analytic solution of *Okada* [1992] for the Parkfield coseismic slip model. The displacement vector at the location of the 14 GPS stations is estimated numerically with the method of *Wang et al.* [2003] (triangles) and with the one developed in this study (circles). The percentage error is plotted as a function of the expected analytical solution for the three components of displacement. The red triangles correspond to a denser sampling of the *Wang et al.* [2003] Green function, which reduces the numerical error.

sufficiently robust for modeling stress-driven afterslip with linear as well as nonlinear rheologies.

Appendix C: Interseismic Slip Rates for a Slip Patch

[57] The response of a rate-strengthening (RS) friction patch to a constant interseismic strain rate obeys

$$\dot{\boldsymbol{\epsilon}}^e + \dot{\boldsymbol{\epsilon}}^i = \dot{\Gamma}\,\mathbf{R} \tag{C1}$$

where $\dot{\boldsymbol{\epsilon}}^e$ and $\dot{\boldsymbol{\epsilon}}^i$ are the elastic and inelastic strain rates, respectively, and $\dot{\Gamma}$ and $\mathbf{R}$ are the amplitude and direction, respectively, of the interseismic strain rate evaluated on the fault patch. After the initial period of transient deformation, the steady state response is inelastic only ($\dot{\boldsymbol{\epsilon}}^e = 0$) and the rate of strain release due to the RS friction patch equals to the strain rate imposed by interseismic loading

$$\dot{\gamma} = \dot{\Gamma} \tag{C2}$$

The strain rate of the slipping patch, $\dot{\gamma}$, is given by

$$\dot{\gamma} = \frac{\dot{s}}{CL} \tag{C3}$$

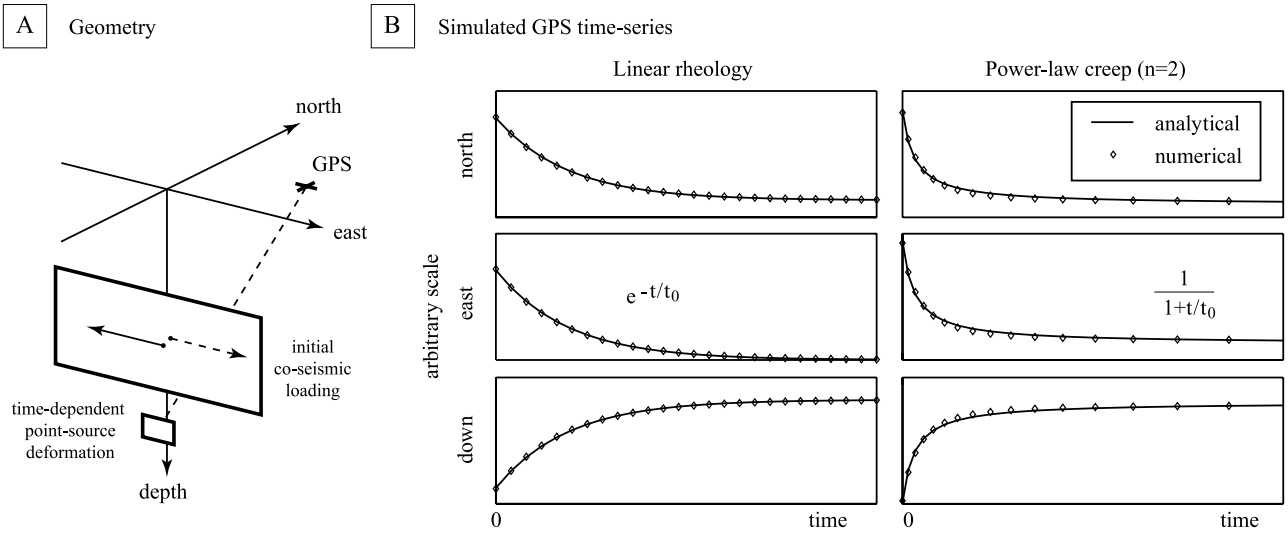

Figure B3. Time-dependent deformation due to frictional sliding on a surface of unit size. (a) The stress on a fault is perturbed due to static slip on an upper segment leading to afterslip. (b) The vector-valued displacement at a surface point driven by the deep afterslip is evaluated numerically using a second-order accurate Runge-Kutta method with adaptive time steps. The forward models compare well with the expected impulse response of linear ($\dot{s} = \Delta\tau/\eta$) and nonlinear ($\dot{s} = A\ (\Delta\tau/G)^n$, here $n = 2$) constitutive laws. The timescale of the synthetic signal is recovered within a 5% error. The adaptive time step is apparent only for the case of a nonlinear evolution law.

where C is a dimensionless parameter depending upon the geometry of the patch and L is the linear dimension of the patch. The RS friction parameter $\dot{s}_0$ is equivalent to parameter V_0 of classic rate-and-state friction for large velocity, but does not represent the ''interseismic'' velocity. Friction parameter $\dot{s}_0$ controls the timescale of deformation transients and the effective ''viscosity'' of the shear zone (see equations (B35) and (B36)).

[58] In case of strike-slip faults, interseismic deformation may be idealized by slip below the seismogenic zone at rates corresponding to the long-term (averaged over multiple earthquake cycles) plate motion [*Savage*, 1990]. The velocity field for a long vertical strike-slip fault locked from the surface to the depth H is

$$\dot{u}_1 = \frac{v}{2\pi}\left[\tan^{-1}\frac{x_2}{H-x_3} + \tan^{-1}\frac{x_2}{H+x_3}\right] \tag{C4}$$

where $\dot{u}_1(x_2, x_3)$ is the along-strike velocity, x_2 is the across-fault distance, x_3 is depth and v is the long-term slip rate. Consider a creeping patch in the locked zone at depth $x_3 < H$. The strain rate imposed on the creeping patch by interseismic loading is

$$\dot{\Gamma} = \frac{v}{2\pi}\frac{H}{H^2 - x_3^2} \tag{C5}$$

Assuming a circular patch of radius L, the creep rate is [*Eshelby*, 1957]

$$\dot{s} = \dot{\Gamma}\,\frac{16}{7\pi}\,L \tag{C6}$$

In the case of a fault slipping at the rate of 33 mm/a with a locking depth of 15 km and a creeping circular patch of radius $L = 2$ km buried at a depth of 5 km, the average creep velocity is $\dot{u}_1 = 1.1$ mm/a.

[59] **Acknowledgments.** We thank Associate Editor John Townend, Allan Rubin, and an anonymous reviewer for their thorough and thoughtful reviews of this manuscript. Our work benefited from discussions with Olivier Castelnau, Eric Dunham, and Nadia Lapusta. This work was supported by NSF though grant EAR-0450035. This paper is SCEC contribution 1270. Numerical codes used in this study are available from the authors.

References

Abramowitz, M., and I. Stegun (1972), *Handbook of mathematical Functions With Formulas, Graphs and Mathematical Tables*, 1046 pp., U.S. Govt. Print. Off., Washington, D. C.

Aki, K., and P. G. Richards (1980), *Quantitative Seismology*, vol. I, W. H. Freeman, New York.

Allmann, B. P., and P. M. Shearer (2007), A high-frequency secondary event during the 2004 Parkfield earthquake, *Science*, *318*, 1279–1283.

Backus, G. (1970), Inference from inadequate and inaccurate data, I, *Proc. Natl. Acad. Sci. U.S.A.*, *65*, 1–7.

Backus, G., and M. Mulcahy (1976), Moment tensors and other phenomenological descriptions of seismic sources-II. Discontinuous displacements, *Geophys. J. R. Astron. Soc.*, *47*, 301–329.

Bakun, W., and T. McEvilly (1984), Recurrence models and Parkfield, California, earthquakes, *J. Geophys. Res.*, *89*, 3051–3058, doi:10.1029/JB089iB05p03051.

Bakun, W. H., and A. G. Lindh (1985), The Parkfield, California, earthquake prediction experiment, *Science*, *229*, 619–624.

Bakun, W. H., et al. (2005), Implications for prediction and hazard assessment from the 2004 Parkfield earthquake, *Nature*, *437*, 969–974, doi:10.1038/nature04067.

Barbot, S., Y. Fialko, and D. Sandwell (2008a), Effect of a compliant fault zone on the inferred earthquake slip distribution, *J. Geophys. Res.*, *113*, B06404, doi:10.1029/2007JB005256.

Barbot, S., Y. Hamiel, and Y. Fialko (2008b), Space geodetic investigation of the coseismic and postseismic deformation due to the 2003 M_w7.2 Altai earthquake: Implications for the local lithospheric rheology, *J. Geophys. Res.*, *113*, B03403, doi:10.1029/2007JB005063.

Barbot, S., Y. Fialko, and D. Sandwell (2009), Three-dimensional models of elasto-static deformation in heterogeneous media, with applications to the Eastern California Shear Zone, *Geophys. J. Int.*, in press.

Burridge, R., and L. Knopoff (1964), Body force equivalents for seismic dislocations, *Bull. Seismol. Soc. Am.*, *54*, 1875–1888.

Byerlee, J. (1978), Friction of rock, *Pure Appl. Geophys.*, *116*, 615–626.

Dieterich, J. H. (1992), Earthquake nucleation on faults with rate- and state-dependent strength, *Tectonophysics*, *211*, 115–134, doi:10.1016/0040-1951(92)90055-B.

Dieterich, J. H. (1994), A constitutive law for rate of earthquake production and its application to earthquake clustering, *J. Geophys. Res.*, *99*, 2601–2618, doi:10.1029/93JB02581.

Dong, D., P. Fang, Y. Bock, F. Webb, L. Prawirodirdjo, S. Kedar, and P. Jamason (2006), Spatiotemporal filtering using principal component analysis and Karhunen-Loeve expansion approaches for regional GPS network analysis, *J. Geophys. Res.*, *111*, B03405, doi:10.1029/2005JB003806.

Eshelby, J. D. (1957), The determination of the elastic field of an ellipsiodal inclusion, and related problems, *Proc. R. Soc. London, Ser. A*, *241*, 376–396.

Evans, B., and D. L. Kohlstedt (1995), Rheology of rocks, in *Rock Physics and Phase Relations: A Handbook of Physical Constants*, *AGU Ref. Shelf*, edited by T. J. Ahrens, pp. 148–165, AGeophys. Union, Washington, D. C.

Fialko, Y. (2004a), Probing the mechanical properties of seismically active crust with space geodesy: Study of the coseismic deformation due to the 1992 M_w7.3 Landers (southern California) earthquake, *J. Geophys. Res.*, *109*, B03307, doi:10.1029/2003JB002756.

Fialko, Y. (2004b), Evidence of fluid-filled upper crust from observations of postseismic deformation due to the 1992 M_w7.3 Landers earthquake, *J. Geophys. Res.*, *109*, B08401, doi:10.1029/2004JB002985.

Fialko, Y. (2007), Fracture and frictional mechanics—Theory, in *Treatise on Geophysics*, vol. 4, Earthquake Seismology, edited by H. Kanamori, pp. 83–106, Elsevier, Oxford, U. K.

Fialko, Y., D. Sandwell, D. Agnew, M. Simons, P. Shearer, and B. Minster (2002), Deformation on nearby faults induced by the 1999 Hector Mine earthquake, *Science*, *297*, 1858–1862, doi:10.1126/science.1074671.

Fialko, Y., D. Sandwell, M. Simons, and P. Rosen (2005), Three-dimensional deformation caused by the Bam, Iran, earthquake and the origin of shallow slip deficit, *Nature*, *435*, 295–299, doi:10.1038/nature03425.

Freed, A. M. (2007), Afterslip (and only afterslip) following the 2004 Parkfield, California, earthquake, *Geophys. Res. Lett.*, *34*, L06312, doi:10.1029/2006GL029155.

Freed, A. M., and R. Bürgmann (2004), Evidence of power-law flow in the Mojave desert mantle, *Nature*, *430*, 548–551, doi:10.1038/nature02784.

Freed, A. M., R. Bürgmann, E. Calais, J. Freymueller, and S. Hreinsdttir (2006), Implications of deformation following the 2002 Denali, Alaska, earthquake for postseismic relaxation processes and lithospheric rheology, *J. Geophys. Res.*, *111*, B01401, doi:10.1029/2005JB003894.

Garofalo, F. (1975), *Fundamentals of Creep and Creep-Rupture in Metals*, MacMillan, New York.

Hamiel, Y., and Y. Fialko (2007), Structure and mechanical properties of faults in the North Anatolian Fault system from InSAR observations of coseismic deformation due to the 1999 Izmit (Turkey) earthquake, *J. Geophys. Res.*, *112*, B07412, doi:10.1029/2006JB004777.

Harris, R. A., and J. R. Arrowsmith (2006), Introduction to the special issue on the 2004 Parkfield earthquake and the Parkfield Earthquake Prediction Experiment, *Bull. Seism. Soc. Am.*, *96*, S1–S10, doi:10.1785/0120050831.

Hsu, Y.-J., M. Simons, J.-P. Avouac, J. Galetzka, K. Sieh, M. Chlieh, D. Natawidjaja, L. Prawirodirdjo, and Y. Bock (2006), Frictional afterslip following the 2005 Nias-Simeulue earthquake, Sumatra, *Science*, *312*, 1921–1926, doi:10.1126/science.1126960.

Johanson, I. A., E. J. Fielding, F. Rolandone, and R. Burgmann (2006), Coseismic and postseismic slip of the 2004 Parkfield earthquake from space-geodetic data, *Bull. Seismol. Soc. Am.*, *96*, S269–S282, doi:10.1785/0120050818.

Johnson, K. M., R. Bürgmann, and K. Larson (2006), Frictional properties on the San Andreas fault near Parkfield, California, inferred from models of afterslip following the 2004 earthquake, *Bull. Seismol. Soc. Am.*, *96*, S321–S338, doi:10.1785/0120050808.

Jonssón, S., P. Segall, R. Pedersen, and G. Björnsson (2003), Post-earthquake ground movements correlated to pore-pressure transients, *Nature*, *424*, 179–183, doi:10.1038/nature01776.

Kanamori, H., and D. L. Anderson (1975), Theoretical basis of some empirical relations in seismology, *Bull. Seismol. Soc. Am.*, *65*, 1073–1095.

Kohlstedt, D. L., B. Evans, and S. J. Mackwell (1995), Strength of the lithosphere: Constraints imposed by laboratory experiments, *J. Geophys. Res.*, *100*, 17,587–17,602, doi:10.1029/95JB01460.

Langbein, J. (2008), Noise in GPS displacement measurements from southern California and southern Nevada, *J. Geophys. Res.*, *113*, B05405, doi:10.1029/2007JB005247.

Langbein, J., and Y. Bock (2004), High-rate real-time GPS network at Parkfield: Utility for detecting fault slip and seismic displacements, *Geophys. Res. Lett.*, *31*, L15S20, doi:10.1029/2003GL019408.

Langbein, J., J. R. Murray, and H. A. Snyder (2006), Coseismic and initial postseismic deformation from the 2004 Parkfield, California, earthquake, observed by Global Positioning System, electronic distance meter, creepmeters, and borehole strainmeters, *Bull. Seismol. Soc. Am.*, *96*, S304–S320, doi:10.1785/0120050823.

Lapusta, N., J. R. Rice, Y. Ben-Zion, and G. Zheng (2000), Elastodynamic analysis for slow tectonic loading with spontaneous rupture episodes on faults with rate- and state-dependent friction, *J. Geophys. Res.*, *105*, 23,765–23,789.

Lisowski, M., J. Savage, and W. H. Prescott (1991), The velocity field along the San Andreas fault in central and southern California, *J. Geophys. Res.*, *96*, 8369–8389, doi:10.1029/91JB00199.

Liu, P., S. Custudio, and R. J. Archuleta (2006), Kinematic inversion of the 2004 m 6.0 Parkfield earthquake including an approximation to site effects, *Bull. Seismol. Soc. Am.*, *96*, S143–S158, doi:10.1785/0120050826.

Love, A. E. H. (1927), *A Treatise on the Mathematical Theory of Elasticity*, Cambridge Univ. Press, Cambridge, U. K. (Reprinted, Dover, New York, 1944.)

Malvern, L. E. (1969), *Introduction to the Mechanics of a Continuum Medium*, 713 pp., Prentice-Hall, Englewood Cliffs, N. J.

Marone, C., B. C. Raleigh, and C. H. Scholz (1990), Frictional behavior and constitutive modeling of simulated fault gouge, *J. Geophys. Res.*, *95*, 7007–7026.

Marone, C., C. Scholz, and R. Bilham (1991), On the mechanics of earthquake afterslip, *J. Geophys. Res.*, *96*, 8441–8452, doi:10.1029/91JB00275.

Marone, C. J. (1998), Laboratory-derived friction laws and their application to seismic faulting, *Annu. Rev. Earth Planet. Sci.*, *26*, 643–696, doi:10.1146/annurev.earth.26.1.643.

Mavko, G. M. (1981), Mechanics of motion on major faults, *Annu. Rev. Earth Planet. Sci.*, *9*, 81–111, doi:10.1146/annurev.ea.09.050181.000501.

McClellan, J., T. Parks, and L. Rabiner (1973), A computer program for designing optimum FIR linear phase digital filters, *IEEE Trans. Audio Electroacoust.*, *21*, 506–526.

Menke, W. (1984), *Geophysical Data Analysis, Discrete Inverse Theory*, Elsevier, New York.

Montési, L. G. J. (2004), Controls of shear zone rheology and tectonic loading on postseismic creep, *J. Geophys. Res.*, *109*, B10404, doi:10.1029/2003JB002925.

Montési, L. G. J., and G. Hirth (2003), Grain size evolution and the rheology of ductile shear zones: From laboratory experiments to postseismic creep, *Earth Planet. Sci. Lett.*, *211*, 97–110, doi:10.1016/S0012-821X(03)00196-1.

Morrow, C., and D. A. Lockner (2001), Hayward fault rocks: Porosity, density and strength measurements, *U.S. Geol. Surv. Open File Rep., 01-421*.

Morrow, C., B. Radney, and J. Byerlee (1992), Frictional strength and the effective pressure law of montmorillonite and illite clays, in *Fault Mechanics and Transport Properties of Rocks*, *Int. Geophys. Ser.*, vol. 51, edited by B. Evans and T.-f. Wong, pp. 69–88, Academic, London.

Murray, J., and J. Langbein (2006), Slip on the San Andreas fault at Parkfield, California, over two earthquake cycles, and the implications for seismic hazard, *Bull. Seismol. Soc. Am.*, *96*, S283–S303, doi:10.1785/0120050820.

Murray, J. R., P. Segall, P. Cervelli, W. Prescott, and J. Svarc (2001), Inversion of GPS data for spatially variable slip-rate on the San Andreas Fault near Parkfield, CA, *Geophys. Res. Lett.*, *28*, 359–362.

Nemat-Nasser, S. (2004), *Plasticity. A Treatise on Finite Deformation of Heterogeneous Inelastic Materials*, Cambridge Univ. Press, New York.

Nemat-Nasser, S., and M. Hori (1999), *Micromechanics: Overall Properties of Heterogeneous Materials*, 2nd ed., Elsevier, New York.

Nur, A., and G. Mavko (1974), Postseismic viscoelastic rebound, *Science*, *183*, 204–206.

Okada, Y. (1992), Internal deformation due to shear and tensile faults in a half-space, *Bull. Seismol. Soc. Am.*, *82*, 1018–1040.

Parker, R. L. (1994), *Geophysical Inverse Theory*, Princeton Univ. Press, Princeton, N. J.

Peltzer, G., P. Rosen, F. Rogez, and K. Hudnut (1998), Poroelastic rebound along the Landers 1992 earthquake surface rupture, *J. Geophys. Res.*, *103*, 30,131–30,145.

Perfettini, H., and J.-P. Avouac (2004), Postseismic relaxation driven by brittle creep: A possible mechanism to reconcile geodetic measurements and the decay rate of aftershocks, application to the Chi-Chi earthquake, Taiwan, *J. Geophys. Res.*, *109*, B02304, doi:10.1029/2003JB002488.

Perfettini, H., and J.-P. Avouac (2007), Modeling afterslip and aftershocks following the 1992 Landers earthquake, *J. Geophys. Res.*, *112*, B07409, doi:10.1029/2006JB004399.

Pollitz, F. F., G. Peltzer, and R. Bürgmann (2000), Mobility of continental mantle: Evidence from postseismic geodetic observations following the 1992 Landers earthquake, *J. Geophs. Res.*, *105*, 8035–8054.

Preisendorfer, R. W., and C. D. Mobley (1988), *Principal Component Analysis in Meteorology and Oceanography*, *Develop Atmos. Sci.*, vol. 17, Elsevier, New York.

Rice, J. R., N. Lapusta, and K. Ranjith (2001), Rate and state dependent friction and the stability of sliding between elastically deformable solids, *J. Mech. Phys. Solids*, *49*, 1865–1898, doi:10.1016/S0022-5096(01)00042-4.

Roberts, D. C., and D. L. Turcotte (2000), Earthquakes: Friction or a plastic instability?, *Geocomplexity and the Physics of Earthquakes*, *Geophys. Monogr. Ser.*, vol. 120, edited by J. B. Rundle, D. L. Turcotte, and W. Klein, pp. 97–103, Washington, D. C.

Ruina, A. (1983), Slip instability and state variable friction laws, *J. Geophys. Res.*, *88*, 10,359–10,370.

Savage, J. C. (1990), Equivalent strike-slip earthquakes cycles in half-space and lithosphere-asthenosphere earth models, *J. Geophys. Res.*, *95*, 4873–4879, doi:10.1029/JB095iB04p04873.

Savage, J. C., and S.-B. Yu (2007), Postearthquake relaxation and aftershock accumulation linearly related after the 2003 *M* 6.5 Chengkung, Taiwan, and the 2004 *M* 6.0 Parkfield, California, earthquakes, *Bull. Seismol. Soc. Am.*, *97*, 1632–1645, doi:10.1785/0120070069.

Savage, J. C., M. Lisowski, and J. L. Svarc (1994), Postseismic deformation following the 1989 (M = 7.1) Loma Prieta, California, earthquake, *J. Geophys. Res.*, *99*, 13,757–13,765, doi:10.1029/94JB00507.

Savage, J. C., J. L. Svarc, and S.-B. Yu (2007), Postseismic relaxation and aftershocks, *J. Geophys. Res.*, *112*, B06406, doi:10.1029/2006JB004584.

Scholz, C. H. (1990), *The Mechanics of Earthquakes and Faulting*, 439 pp., Cambidge Univ. Press, New York.

Scholz, C. H. (1998), Earthquakes and friction laws, *Nature*, *391*, 37–42, doi:10.1038/34097.

Scholz, C. H. (2002), *The Mechanics of Earthquakes and Faulting*, 2nd ed., 496 pp., Cambidge Univ. Press, New York.

Shearer, P. M. (1999), *Introduction to Seismology*, Cambridge University Press, New York.

Stuart, W. D., and T. E. Tullis (1995), Fault model for preseismic deformation at Parkfield, California, *J. Geophys. Res.*, *100*, 24,079–24,099, doi:10.1029/95JB02517.

Tarantola, A. (2004), *Inverse Problem Theory and Methods for Model Parameter Estimation*, Soc. for Ind. and Appl. Math, Philadelphia, Pa.

Tsenn, M. C., and N. L. Carter (1987), Upper limits of power law creep of rocks, *Tectonophysics*, *136*, 1–26, doi:10.1016/0040-1951(87)90332-5.

Waldhauser, F., W. L. Ellsworth, D. P. Schaff, and A. Cole (2004), Streaks, multiplets, and holes: High-resolution spatio-temporal behavior of Parkfield seismicity, *Geophys. Res. Lett.*, *31*, L18608, doi:10.1029/2004GL020649.

Wang, R., F. L. Martin, and F. Roth (2003), Computation of deformation induced by earthquakes in a multi-layered elastic crust - FORTRAN programs EDGRN/EDCMP, *Comput. Geosci.*, *29*, 195–207, doi:10.1016/S0098-3004(02)00111-5.

Wdowinski, S., Y. Bock, J. Zhang, P. Fang, and J. Genrich (1997), Southern California permanent GPS geodetic array: Spatial filtering of daily positions for estimating coseismic and postseismic displacements induced by the 1992 Landers earthquake, *J. Geophys. Res.*, *102*, 18,057–18,070.

Weertman, J., and J. R. Weertman (1964), *Elementary Dislocation Theory*, Macmillan, New York.

Weertman, J., and J. R. Weertman (1975), High temperature creep of rock and mantle viscosity, *Annu. Rev. Earth Planet. Sci.*, *3*, 293–315.

Williams, S. D. P., Y. Bock, P. Fang, P. Jamason, R. M. Nikolaidis, L. Prawirodirdjo, M. Miller, and D. J. Johnson (2004), Error analysis of continuous GPS position time series, *J. Geophys. Res.*, *109*, B03412, doi:10.1029/2003JB002741.

S. Barbot, Y. Bock, and Y. Fialko, Institute of Geophysics and Planetary Physics, Scripps Institution of Oceanography, University of California, San Diego, 9500 Gilman Drive, MS 0225, La Jolla, CA 92093-0225, USA. (sbarbot@ucsd.edu)